

State-resolved transport collision integrals for the O + O₂ systemSharanya Subramaniam *Department of Mechanical Science and Engineering, University of Illinois at Urbana-Champaign,
Urbana, Illinois 61801, USA*Richard L. Jaffe *NASA Ames Research Center, Moffett Field, California 94035, USA*Kelly A. Stephani **Department of Mechanical Science and Engineering,
and University of Illinois at Urbana-Champaign, Urbana, Illinois 61801, USA*(Received 4 April 2020; accepted 14 September 2020;
published 11 November 2020)

There has been a growing interest in implementing state-resolved models for flowfield calculations of high-speed reentry applications that are characterized by regions of strong nonequilibrium. To this end, the present work provides a technique to rigorously compute transport collision integrals for vibrationally excited molecules. Collision dynamics calculations are extended to include state-to-state (StS) effects, and vibrationally resolved transport collisional quantities including scattering angles, cross sections, and collision integrals are computed for the O + O₂ system using potential energy surfaces (PESs) by Varga *et al.* [*J. Chem. Phys.* **147**, 154312 (2017)]. From the nine surfaces provided by Varga *et al.*, the “surface-averaged” collision integrals are computed for the oxygen system, and Gupta-Yos-style fits to the data are provided. It is found that the StS collision integrals depend not only on the vibrational state of the molecule, but also on the spin and spatial degeneracy associated with the PES that governs the interaction. Comparison of the collision integrals from the Varga *et al.* surfaces with those generated from the Varandas and Pais PES [*Mol. Phys.* **65**, 843 (1988)] shows significant differences at highly excited vibrational states. The highly attractive nature of the Varandas and Pais surface leads to a monotonic increase in the collision integral values with vibrational excitation of O₂, while the surface-averaged state-based collision integral values computed from the comparatively repulsive Varga *et al.* set of surfaces generally increase with vibrational excitation for temperatures up to 6000 K, and decrease with vibrational excitation at higher temperatures. Additionally, due to this nontrivial dependence of the collision integrals on the vibrational state of O₂, simple empirical models are found to be unable to correctly estimate vibrational state-based collision integrals. Differences as high as 80% are obtained between the model predictions and values computed directly from the underlying PES. Evaluation of vibrationally resolved viscosity and translational thermal conductivity for the O + O₂ system under equilibrium conditions indicate that both these transport coefficients depend on the vibrational excitation of O₂, with the contribution of the excited vibrational states increasing with rising temperature.

DOI: [10.1103/PhysRevFluids.5.113402](https://doi.org/10.1103/PhysRevFluids.5.113402)

*ksteph@illinois.edu

I. INTRODUCTION

Hypersonic entry of space vehicles into planetary atmospheres is characterized by a wide variety of coupled chemical and physical processes spanning a range of timescales. The high, directed kinetic energy of the flow is converted to thermal energy through particle collisions, creating shock layers characterized by high temperature and exhibiting internal energy excitation, dissociation/recombination, or ionization [1]. At the same time, a low density wake is formed as the flow expands downstream of the vehicle forebody, presenting thermal and chemical nonequilibrium features. To capture and quantify the influence of these nonequilibrium phenomena, additional governing equations for the various internal energy modes of gas molecules are included in computational fluid dynamics (CFD). With a view to providing consistent closure to this modified set of governing equations, the present work focuses on computing transport collision integrals arising due to interactions between molecular and atomic oxygen. These collision integrals [2] play a crucial role in calculating various transport coefficients—mass diffusion, thermal conductivity, and viscosity—that carry collisional information into the macroscopic flow processes.

A popular approach to model nonequilibrium effects within CFD is the use of multitemperature (MT) models [3–6]. These models assume that for all species present in a gas mixture, the population within each internal energy mode (rotational, vibrational, electronic) follows an equilibrium Boltzmann distribution at a mode-specific temperature (T_{rot} , T_{vib} , T_{elec}). The temporal and spatial evolution of energy in each internal mode is achieved by means of a separate energy equation, in addition to mass, momentum, and total energy conservation equations. Chemical reactions are accounted for by evaluating the macroscopic rate constant at an “effective temperature” based on an empirical relation involving the various temperatures that influence a reaction [7,8]. Empirical relations are also used to treat the relaxation process between the internal and translational energy modes [9,10]. The above described MT model, however, provides an accurate solution only when the population within the internal energy modes may be approximated by an equilibrium Boltzmann distribution [11].

To allow for internal energy distributions that are in strong nonequilibrium like those observed in the shock layer of a hypersonic flow [12,13], high-fidelity state-to-state (StS) models need to be employed. In state-based models [14], each internal energy level is treated as a separate “pseudo-” species and is characterized by an equilibrium Maxwellian distribution function in velocity space, defined at the gas translational temperature, T . Varying levels of fidelity can be obtained by choosing the internal energy modes that need to be modeled in a state-based fashion. For instance, a number of studies allow for nonequilibrium in the vibrational energy distribution, while assuming that the rotational modes equilibrate rapidly to the translational temperature [14–16]. Typically, the translational mode is assumed to be at or very close to equilibrium. If translational nonequilibrium in the flowfield [17–21] also needs to be captured, noncontinuum approaches like direct simulation Monte Carlo (DSMC) [22–29] or hybrid CFD-DSMC [30–33] models may be employed. Yet another technique available for modeling noncontinuum flows is the direct molecular simulation (DMS) approach, where the collision models used within DSMC are replaced by trajectory calculations [34,35]. However, in the present work, we assume that the velocity distribution function of each species is near equilibrium and that the continuum approximation holds.

Considerable work has been carried out in developing and incorporating state-based modeling into the CFD framework. First, the Navier-Stokes governing equations have been recast to allow for flow simulations with non-Boltzmann internal energy distributions [12–14,16,36–42]. To accurately model the kinetics source terms that appear in these equations, extensive databases have been generated through quasiclassical trajectory (QCT) simulations for StS rate coefficients describing excitation and dissociation kinetics [43–48]. These QCT calculations require the interaction potential between the chemical species, i.e., the potential energy surface (PES), as an input. Recent advances in computational chemistry have allowed for the development of high-fidelity *ab initio* PESs for a number of chemical systems [49–56], thus enabling very accurate estimation of their StS rate coefficients. Similarly, the challenge of computational cost that

state-based CFD problems pose is being addressed through the development of coarse-graining techniques [57–62].

While significant effort has been made to develop and implement a computationally tractable, state-based CFD framework with StS reaction kinetics information, a complete StS description of high-speed, viscous flows requires that the transport terms present in the governing equations are also accounted for in a state-based manner. Towards this end, Nagnibeda and Kustova [14,15] have outlined a technique for computing state-based transport coefficients with StS treatment of the vibrational mode, with the rotational mode following a Boltzmann distribution at the translational temperature. This approach yields a large number of linear algebraic equations that need to be solved at all spatial locations in the flowfield at each time instant, and so a simplified procedure has been proposed [63,64] where the dependence of transport collision integrals on the internal (vibrational) level of the molecule is ignored in flowfield calculations [65].

In the study by Bruno *et al.* [66] a preliminary assessment of the influence of vibrational level on collision integrals was carried out by assuming that atoms and molecules in the gas interact based on the hard sphere model [22]. Further, variation in the molecule's diameter with vibrational level was obtained using an analytical expression based on a Morse or a Tietz-Hua model for the molecule [67]. Some works have also used the approximate hard sphere model [68,69] or phenomenological interaction potentials [70] for transport collision integrals, along with analytical estimates based on a Morse potential to account for variation in molecular diameter with vibrational excitation [71]. However, for consistent flow calculations, both high-temperature transport and reaction kinetics should be computed from the same *ab initio* PESs. Only recently, such a study for a vibrationally resolved $N_2 + O$ system has been performed by Luo *et al.* [72] using QCT calculations, while assuming that the population within the rotational energy mode follows an equilibrium Boltzmann distribution at the translational temperature.

The $O + O_2$ system has been extensively studied with an emphasis on state-based reaction kinetics [46–48,73–77]. Hence, obtaining its state-based collision integrals in a rigorous manner is necessary to complete the StS formulation, comprising state-resolved kinetics and transport. Therefore, in the current work, as a first step, we compute the *vibrationally resolved* collision integrals for the oxygen system from two sets of PESs, by Varandas and Pais [49] and by Varga *et al.* [54]. The set of surfaces proposed by Varga *et al.* [54] includes all spin and spatial degeneracies in the $O + O_2$ system and was specifically constructed to capture the processes involved in high-energy collisions that are important in hypersonic flows. Prior to the availability of the Varga *et al.* set of surfaces, the single, ground-state singlet surface by Varandas and Pais [49] has been PES of choice to study the $O + O_2$ system, and a number of studies relevant to hypersonic reentry have been performed based on it [27,47,48,78,79]. However, this surface, having the lowest statistical weight, accounts for only 1/27 of total collisions. Therefore, it is instructive to compare the state-based collision integrals between this conventionally employed surface and the newer set of nine surfaces by Varga *et al.* to better highlight the differences that arise by including the more relevant, higher statistical weight surfaces. Finally, the collision integrals computed from the nine Varga *et al.* surfaces for each vibrational level are fit as a function of translational temperature. It is worth noting that based on master equation and shock flow studies of the $N_2 + N$ system using *ab initio* PESs, Panesi *et al.* [12,13] have indicated that at high temperatures, the rotational energy distribution can be strongly non-Boltzmann. A more recent work has also indicated that the rotational levels contribute up to 40% of the total energy for dissociation [62]. Thus, if both rotational and vibrational modes are to be treated in a state-based manner, a consistent, rovibrationally resolved transport model will also need to be developed. Therefore, calculations for collision integrals presented in this work will be extended to both rovibrationally resolved as well as coarse-grained systems in future studies.

This paper is structured as follows: Sec. II introduces the approach adopted in the present work to compute the vibrational state-based transport collisional parameters. The two potential energy surfaces employed in this work are described in Sec. III, and the numerical procedure to obtain the various state-resolved transport collisional quantities is outlined. Next, the state-based potentials,

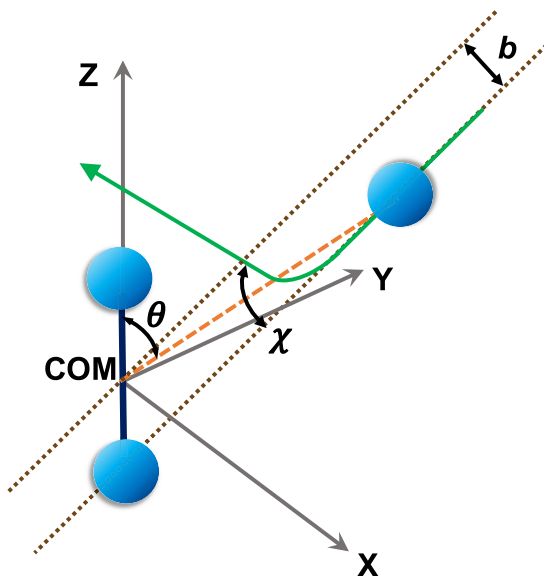


FIG. 1. Atom-molecule collision dynamics. The solid green curve denotes the atom's trajectory, determined by orientation angle, θ . b and χ are the impact parameter and scattering angle, respectively. Reprinted from Sharanya Subramaniam and Kelly A. Stephani, "State-based transport and scattering properties for the $O + O_2$ system," in *AIP Conference Proceedings*, vol. 2132, no. 1 (AIP Publishing LLC, College Park, MD, 2019), with the permission of AIP Publishing.

scattering angles, and collision integrals from more recent Varga *et al.* [54] surfaces are presented in Sec. IV. In Sec. V we discuss the differences in the transport collisional parameters between the Varandas and Pais [49] and the corresponding $1^1A'$ surface of Varga *et al.* [54]. We then compare the vibrationally resolved collision integrals calculated in the present work with those obtained by empirical scaling relations [70], and also provide the "state-averaged" collision integrals under equilibrium and two-temperature conditions. Finally, state-based viscosity and translational thermal conductivity under equilibrium conditions are calculated using the vibrationally resolved collision integrals obtained in this work. Conclusions from the study are presented in Sec. VI.

II. TRANSPORT COLLISIONAL PROPERTIES IN STATE-RESOLVED SYSTEMS

Within the generalized Chapman-Enskog framework extended to rovibrationally resolved, state-based systems [14,80,81], the StS transport coefficients, such as viscosity, diffusion coefficients, and thermal conductivity, provide closure to a first-order solution of the Boltzmann equation. It should be noted that this closure is defined only over the rapid collisional processes in the system, which for such a state-resolved case are elastic collisions. Therefore these transport coefficients are expanded in a rapidly converging series of Sonine polynomials in relative translational energy, and a key input for their estimation is the knowledge of the state-resolved collision integrals. State-based collision integrals are quantities that capture the influence of particle interaction on the exchange of momentum and energy during a binary collision process. The present work focuses on quantifying the effect of the vibrational state of O_2 on the various transport collisional properties that arise due to interactions with an O atom, namely, the state-based collision integrals, diffusion and viscosity cross sections, and scattering angles.

An atom-diatom collision process is illustrated in Fig. 1. Here the collision is characterized as the interaction between the atom and the center of mass (CoM) of the molecule, i.e., between two point

particles, with the distance r being measured from the molecule's CoM. Assuming only rapid elastic collisions, the conventional process to compute collisional transport quantities [80] is adapted to the StS framework for a specific orientation as shown in Eqs. (1)–(4):

$$r_{min}(b, \varepsilon_{tr}) = \text{root} \left[1 - \frac{b^2}{r^2} - \frac{\varphi_{cid}(r)}{\varepsilon_{tr}} \right], \quad (1)$$

$$\chi_{cid}(b, \varepsilon_{tr}) = \pi - 2b \int_{r_{min}}^{\infty} \frac{dr/r^2}{\sqrt{1 - \frac{b^2}{r^2} - \frac{\varphi_{cid}(r)}{\varepsilon_{tr}}}}, \quad (2)$$

$$\mathcal{Q}_{cid}^{(s)}(\varepsilon_{tr}) = 2\pi \int_0^{\infty} [1 - \cos^s \chi_{cid}(b, \varepsilon_{tr})] b db, \quad (3)$$

$$\Omega_{cid}^{(s,t)}(T) = \left(\frac{kT}{2\pi m_{cd}} \right)^{1/2} \int_0^{\infty} \exp(-\gamma^2) \gamma^{2t+3} \mathcal{Q}_{cid}^{(s)}(\varepsilon_{tr}) d\gamma. \quad (4)$$

Details about the orientation angle value are provided in Sec. IV. In the above equations, χ , $\mathcal{Q}^{(s)}$, and $\Omega^{(s,t)}$ represent the scattering angle, transport cross section, and collision integrals, respectively. The subscripts c and d denote the molecule O_2 and the atom O , respectively, and i represents a specific internal state of O_2 . In the present work, we restrict i to only vibrational states.

The first step in computing the StS collision integrals is evaluating r_{min} , which is the distance of closest approach. This determines the minimum distance between two interacting particles prior to scattering away by an angle χ_{cid} (Fig. 1). Equation (1) indicates that r_{min} is influenced by the impact parameter, b , the relative translational energy of the collision, ε_{tr} , and the interaction potential, $\varphi(r)$. In order to incorporate state-based information into the collision integral calculation, the interaction potential that appears in Eq. (1) has been modified to the *state-based* potential, $\varphi_{cid}(r)$. The method of obtaining this StS potential is described in Sec. III B, and the values are presented in Sec. IV A.

Based on the value of r_{min} , the classical StS scattering angle, χ_{cid} , is computed as a function of b and ε_{tr} , for each vibrational level of the molecule. It should be noted that scattering calculations using quantum and semiclassical approaches have also been performed [82–84]. However, for heavier collision pairs like those considered in this work, the classical scattering calculation is expected to provide reasonable accuracy, and is hence adopted here. The scattering angles are then used in Eq. (3) to obtain the state-resolved transport cross section, $\mathcal{Q}_{cid}^{(s)}$, that is a function of ε_{tr} . The superscript is used to denote the nature of the cross section being evaluated, with $s = 1$ and $s = 2$ denoting the diffusion and viscosity cross sections, respectively. The final step is integrating the state-based cross sections over ε_{tr} to arrive at the StS collision integral values. This integration is performed by averaging over the reduced relative translational energy, $\gamma^2 = \varepsilon_{tr}/kT$, where k is Boltzmann constant and T is the translational temperature. Similar to the cross-section calculations, various orders of the StS collision integrals, $\Omega_{cid}^{(s,t)}$, can be obtained by setting the value of index t appropriately. It should be noted that m_{cd} in Eq. (4) is the reduced mass of the system given by

$$m_{cd} = \frac{m_c m_d}{(m_c + m_d)}. \quad (5)$$

It can be seen from Fig. 1 that the orientation angle, θ , between the colliding molecule and atom can change during the course of a collision. However, as a means of avoiding complete trajectory evaluations, the relative orientation between the atom and molecule is assumed to remain constant during a collision event. The effect of the asymmetrical nature of the interaction potential on the transport collision parameters is instead accounted for by evaluating quantities in Eqs. (1)–(4) at a fixed orientation θ , and then averaging over all orientations [85]:

$$\langle \Omega_{cid}^{(s,t)}(T) \rangle = \frac{1}{2} \int_0^{\pi} \Omega_{cid}^{(s,t)} \sin\theta d\theta. \quad (6)$$

The following sections describe the numerical technique adopted in the present work to evaluate these StS collision integrals for the oxygen system.

III. NUMERICAL PROCEDURE

The primary input in computing the vibrational state-based collisional transport quantities is the interaction potential between the atoms involved, in this case the three O atoms of the O + O₂ system. In the present work, two sets of potential energy surfaces are studied, from Varandas and Pais [49] and Varga *et al.* [54]. Details of the surfaces employed are described in Sec. III A, and the numerical technique adopted to compute the various StS collisional transport quantities is discussed in Sec. III B.

A. Potential energy surfaces for O + O₂

The two sets of interaction potentials adopted for the present study of state-based collision integrals are briefly described below.

(1) *Varandas and Pais [49] surface*: This surface is a hybrid empirical-*ab initio* PES that describes the ground (lowest singlet) state of ozone. The surface is based on the double many-body expansion paradigm, which is a multiproperty fit to both experimental and *ab initio* data, as opposed to the more recent surfaces for O + O₂ interactions [54] which have been generated to fit data obtained completely from *ab initio* calculations. Fitting parameters describing the extended Hartree-Fock (EHF) three-body energy terms of the Varandas and Pais [49] PES are tuned such that they reproduce dissociation energy, geometry, and force field for the equilibrium ozone conformers experimentally obtained by Barbe *et al.* [86]. Similarly, *ab initio* data obtained from Shih *et al.* [87] were used to tune fitting parameters of the EHF three-body terms. However, only a single surface corresponding to the ground singlet state, i.e., 1 ¹A', is provided by Varandas and Pais [49] to capture the interaction between O(³P) + O₂(³Σ_g⁻³).

(2) *Varga *et al.* [54] surfaces*: This is a recently constructed set of nine adiabatic surfaces that provide the interaction potential for collisions between a ground-state O₂ (³Σ_g⁻³) and a ground-state O (³P) atom. The collisional interaction between O and O₂ can proceed along singlet, triplet, and quintet potential energy surfaces. Further, a threefold spatial degeneracy is associated with each spin state that gives rise to two surfaces of A' symmetry and one of A''. Thus, there are nine different potential energy surfaces on which O + O₂ collisions can occur: three singlet surfaces, 1 ¹A', 2 ¹A', 1 ¹A'', three triplet surfaces, 1 ³A', 2 ³A', 1 ³A'', and three quintet surfaces, 1 ⁵A', 2 ⁵A', 1 ⁵A''. The statistical weight associated with each singlet, triplet, and quintet surface is 1/27, 3/27, and 5/27, respectively. Thus, the collisions on the quintet surfaces are most heavily weighted. The 1 ¹A' PES corresponds to the ground electronic state of the ozone molecule, which has a weight of 1/27 (as does the Varandas and Pais [49] surface).

As a representative comparison between the two sets of PESs discussed above, Fig. 2 shows contour plots of a head-on (collinear) collision between the O atom and O₂ molecule as described by the ground state 1 ¹A' surfaces of Varga *et al.* [54] and the Varandas and Pais [49] surface. In both plots, R1 represents the internuclear separation between two bonded O atoms, and R2 is the distance between the approaching atom and the closest O atom for this case of a collinear interaction. Considerable differences can be observed in the two interaction energy contours, especially when R1 and R2 are less than ~3 Å. For example, the interaction potential of Varandas and Pais [49] exhibits two saddle points around R1 ~ 1.4 Å, R2 ~ 2.2 Å, and R1 ~ 2.2 Å, R2 ~ 1.4 Å, which are not observed in the 1 ¹A' surfaces of Varga *et al.* [54]. The manifestation of these differences in terms of transport collisional parameters will be presented in Sec. V.

B. State-based collision integral calculation

The first, and perhaps most important objective for computing state-resolved transport is to incorporate excited vibrational state information via the potential φ_{cid} introduced in Eqs. (1) and (2). The StS potential describes the variation in the system's interaction or potential energy when an O atom is moved along a given orientation from an infinite (large) distance where no interaction occurs, toward the CoM of an O₂ molecule, whose vibrational quantum number is held fixed. Each

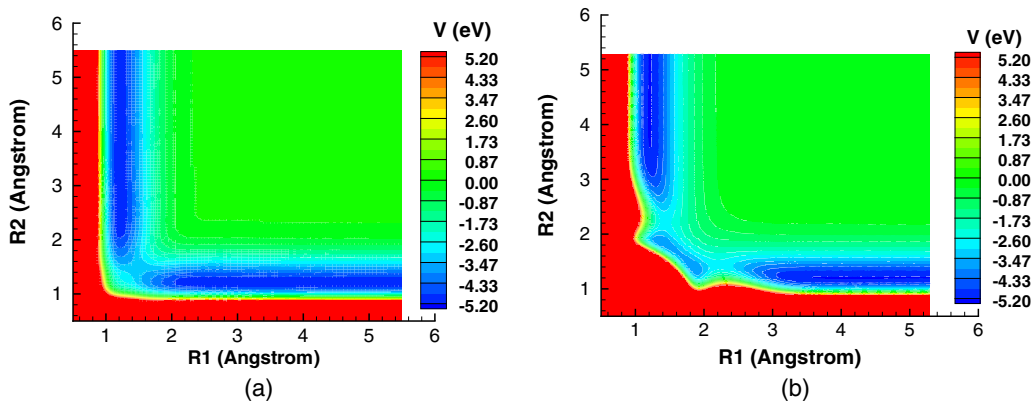


FIG. 2. Interaction potential contours depicting a head-on (collinear) collision between O and O₂ based on the (a) 1¹A' surfaces of Varga *et al.* [54] and (b) Varandas and Pais [49] surface. Reprinted from Sharanya Subramaniam and Kelly A. Stephani, “State-based transport and scattering properties for the O + O₂ system,” in *AIP Conference Proceedings*, vol. 2132, no. 1 (AIP Publishing LLC, College Park, MD, 2019), with the permission of AIP Publishing.

vibrational quantum state of O₂ is therefore characterized by an average bond length to serve as a link between the PES and the StS potential, φ_{cid} . The StS potential is thus a function of the orientation, θ , and position of the approaching atom with respect to the CoM of the molecule whose internuclear separation is held constant. The procedure to estimate this internuclear spacing or average bond length, r_{ave} , is described below.

Based on the two-body O + O potential used to construct the three-body Varga *et al.* [54] PES, the energy eigenvalues for each vibrational level and the minimum and maximum bond lengths are determined for the O₂ molecule using the semiclassical Wentzel-Kramers-Brillouin (WKB) approximation. For this PES, the molecule was found to have 38 vibrational quantum levels corresponding to zero rotation. For each such level, an average bond length is calculated as the arithmetic mean of the minimum and maximum bond lengths. On the other hand, the two-body O + O potential used in the Varandas and Pais [49] O + O₂ surface has 48 vibrational levels for O₂ with zero rotation. The energy eigenvalues of these levels are provided by Andrienko *et al.* [47]. Using these energies and placing the third O atom at an arbitrarily large distance from the O₂ molecule’s center, a root finding procedure is employed to obtain the classical minimum and maximum bond length for each vibrational level of O₂. The average bond length for each vibrational level is then computed as the arithmetic mean of the corresponding minimum and maximum bond length. Finally, by fixing the spacing between the two atoms that form the O₂ molecule to this average bond length, r_{ave} , the StS potential, φ_{cid} , for a given orientation θ , is extracted from the PES as a function of the distance, r of the approaching O atom from the CoM of the O₂ molecule (Fig. 3).

Next, the state-based potentials are used to calculate the distance of closest approach, r_{min} , for an O + O₂ collision with specific values of r_{ave} for a given vibrational level, θ and b . This value is obtained as the outermost root of the function provided in Eq. (1). Although gradient-based root finding methods provide more rapid convergence, they require a very good initial guess for r_{min} and do not guarantee that the resulting root is indeed the outermost one. Hence, in this work, the adaptive step-size routine proposed by Colonna and Laricchiuta [88] has been extended to a vibrational state-resolved formulation. Similarly, the integrals in Eqs. (2)–(4) are also evaluated using an adaptive step-size and fractal integration routine outlined by Colonna and Laricchiuta [88]. However, each integral presents its own unique numerical challenges. While the upper limit of integration for the scattering angle integral in Eq. (2) is chosen as 10⁶ bohr, the integrand results

in an integrable singularity at the lower limit of integration, r_{min} . Hence, the integral in Eq. (2) is computed numerically only up to a lower limit of $r_{min} + \delta$, where δ is a small number. Near the singularity, the integrand in Eq. (2) is evaluated analytically [88]. Similarly, nonintegrable singularities are also observed in Eq. (2) for which the interaction results in “orbiting.” Physically, molecular orbiting manifests as the interacting particles (atom or molecule) revolve about their common CoM. The value of χ_{cid} becomes a large negative number at these conditions. In such cases, the integration routine steps across this nonintegrable singularity. As a result of the discontinuity in χ_{cid} , the transport cross-section integrand given by Eq. (3) exhibits rapid oscillations. Owing to these numerical difficulties, the scattering angle and transport cross-section calculations have been validated [89] against available data for simple potentials [80,88]. It should also be noted that the lower limit of the integral in Eq. (3) is chosen as 10^{-6} bohr, and the upper limit is determined by defining a threshold for χ_{cid} . Thus, in this work, the upper limit, b_{max} is such that for $b > b_{max}$, the value of $\chi_{cid} < 0.001$ rad. For the transport collision integral described by Eq. (4), the limits of integration are taken as 10^{-5} eV and 10 eV, respectively. The integration routine developed in this work has been validated with data from Stallcop *et al.* [84], the details of which are presented in Fig. 6(a).

IV. RESULTS

The numerical procedure described in Sec. III is employed to compute the vibrational state-based transport collisional quantities for the O + O₂ system. While only three surfaces were presented in our preliminary study [81], all nine surfaces provided by Varga *et al.* [54] are included in this work. In Sec. IV A, the state-resolved potential, $\varphi_{cid}(r)$, which serves as the main input for the transport properties, is presented. The StS scattering angle profiles and the diffusion collision integrals normalized by the hard-sphere factor [80,84], $\sigma^2\Omega^{(1,1)*}$ are provided in Secs. IV B and IV C, respectively. Details of the state-based distance of closest approach, diffusion and viscosity cross sections, and viscosity collision integrals are provided in the Supplemental Material [90]. For all plots presented in this section, the state-based quantities are provided for six representative vibrational states, $i = 0, 10, 25, 30, 35,$ and 37 . The relative orientation between the O atom and the O₂ molecule, unless otherwise mentioned, is kept constant by setting $\theta = 54.74^\circ$ as shown in Fig. 1. This corresponds to the effective orientation proposed by Stallcop *et al.*, [84] who showed that the collision integrals computed at this effective orientation provide very good agreement with those obtained by averaging over all orientations. The applicability of this simplification technique to the state-based framework is assessed in Sec. 4 of the Supplemental Material [90].

A. State-based interaction potentials

Figure 3 shows the vibrational state-based potential for all nine surfaces of Varga *et al.* [54]. Each curve in the plots corresponds to a particular vibrational level of the O₂ molecule, which is described by an average bond length as discussed in Sec. III. The StS interaction potential is plotted as a function of r , defined as the distance of the approaching O atom from the CoM of the O₂ molecule. The nature of the StS potential differs significantly between surfaces and is thus affected by both the spin and spatial degeneracies in the O + O₂ system. Further, the influence of vibrational state of O₂ on the interaction potential depends on the surface along which the collisional process occurs.

Distinct StS potentials are observed as the vibrational state of the molecule is changed on the $1^1A'$, $1^1A''$, $1^3A'$, and $1^3A''$ surfaces. With increasing vibrational excitation of the molecule, the StS potential curve becomes deeper and exhibits a larger attractive region. This is attributed to the increased bond length of the molecule as the vibrational level increases. The repulsive portion of the StS potential at small values of r exhibits similar trends across vibrational levels of O₂. However, on the highest spin surfaces ($1^5A'$ and $1^5A''$), a strong repulsive barrier develops, starting at a relatively large distance of ~ 2.5 Å between the incoming O and the CoM of O₂ for the specified orientation of $\theta = 54.74^\circ$ (Fig. 1). With the exception of $i = 37$, the StS interaction potential in the

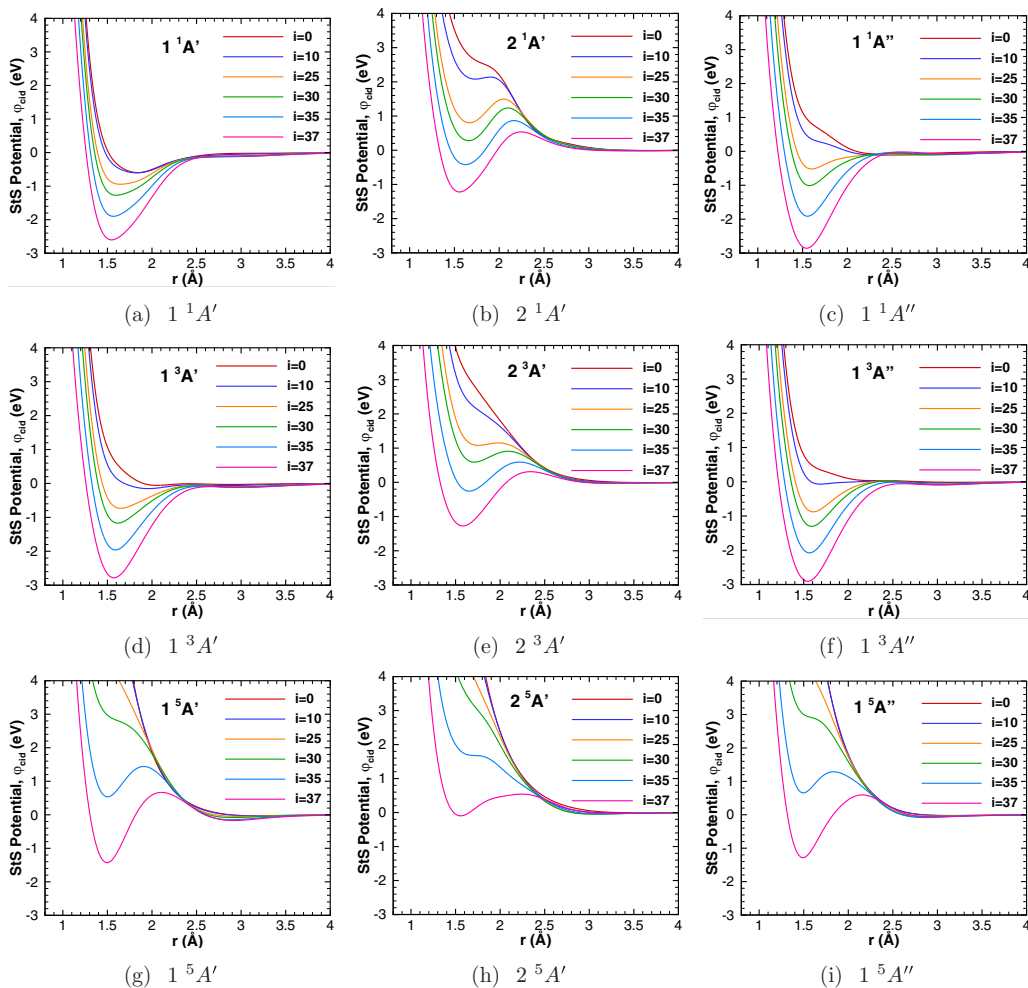


FIG. 3. State-based potentials for six vibrational levels of O_2 , as a function of the distance of the approaching O atom from the CoM of the molecule. Panels (a)–(c) correspond to the singlet state, (d)–(f) being the triplet surfaces, and (g)–(i) represent the quintet surfaces.

system follows a similar strongly repulsive curve for all vibrational states of the molecule. For the vibrational state $i = 37$, the StS potential exhibits only a short repulsive barrier around $\sim 2\text{--}2.5 \text{ \AA}$ and subsequently becomes attractive with well depths approaching 1.5 eV for the $1^5A'$ and $1^5A''$ surfaces. For the first excited adiabatic surfaces for all spin states ($2^1A'$, $2^3A'$, $2^5A'$), a repulsive barrier develops at $\sim 2.5 \text{ \AA}$ between the O atom and the CoM of the O_2 molecule. However, the height of this barrier reduces as the O_2 becomes vibrationally excited, allowing for attractive forces to influence the collision trajectory for highly excited O_2 molecules. Figures 3(b), 3(e), and 3(h) also indicate that as the spin states increase, the StS potentials tend to become more repulsive. Finally, the influence of the vibrational state of O_2 along the first excited ($2^x A'$) surface decreases from the singlet towards the quintet state.

B. State-based scattering angles

Scattering angle calculations are performed for the $\text{O} + \text{O}_2$ system along all nine Varga *et al.* [54] surfaces. While calculations were performed for two values of relative translational energy between

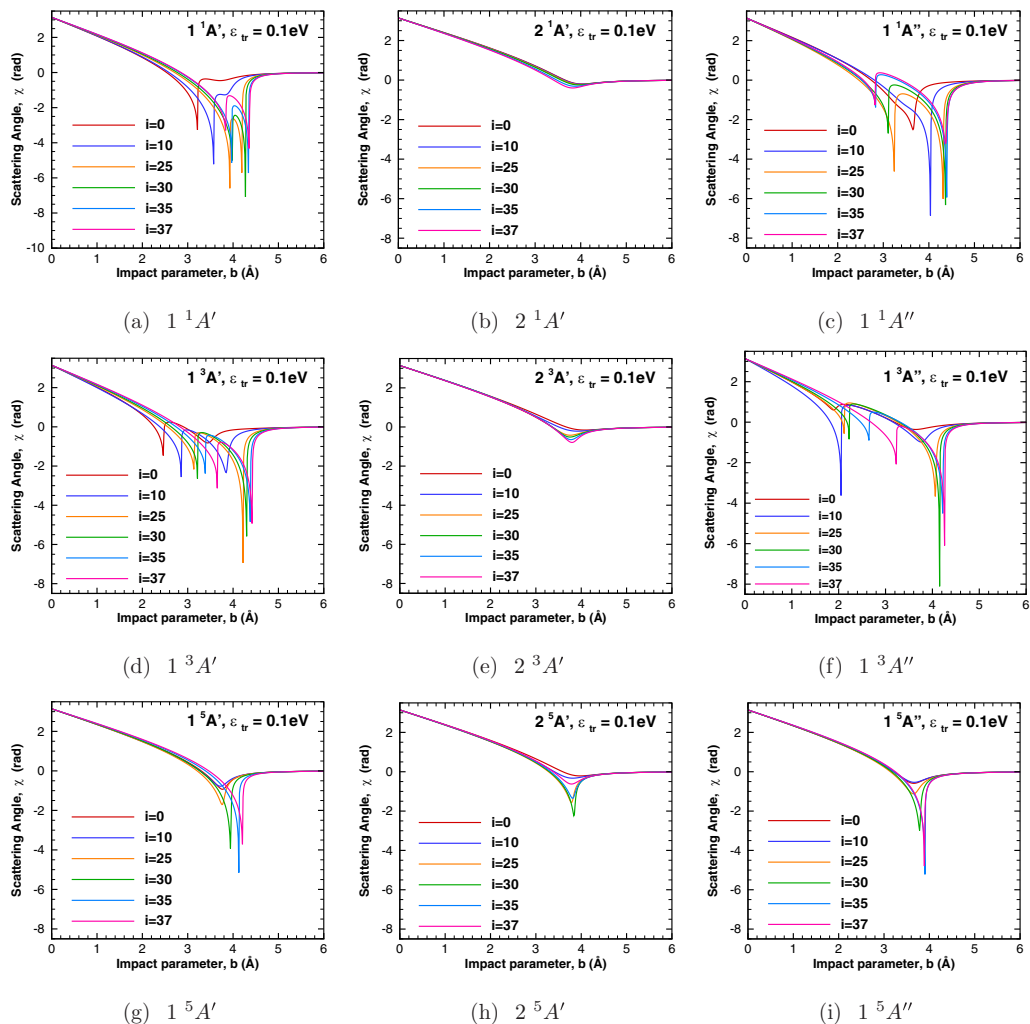


FIG. 4. State-based scattering angle vs impact parameter at different ε_{tr} , for six vibrational levels of O_2 at relative translational energy, $\varepsilon_{tr} = 0.1$ eV. Panels (a)–(c) correspond to the singlet state, (d)–(f) the triplet surfaces, and (g)–(i) the quintet surfaces.

O and O_2 , namely, $\varepsilon_{tr} = 10$ and 0.1 eV, for sake of brevity, only scattering results for $\varepsilon_{tr} = 0.1$ eV are presented here. For the $\varepsilon_{tr} = 10$ eV case, it was found that the scattering angles at low impact parameter values are essentially independent of the vibrational state of O_2 , due to the similar nature of the repulsive portion of the StS potential that influences these interactions. For larger b values, the scattering angles became less repulsive with vibrational excitation of O_2 .

Figure 4 shows the scattering angles on the y axis plotted as a function of impact parameter, for $\varepsilon_{tr} = 0.1$ eV. Note that positive values of χ indicate repulsive scattering, $\chi \approx 0$ represents cases with negligible scattering, and negative values for χ indicate that the attractive portion of the interaction potential has influenced the postcollision trajectory [91]. Similar to the StS potential plots in Fig. 3, each curve in these plots corresponds to O_2 at the specified vibrational level.

A striking feature of the StS scattering angle calculations are sharp dips observed in the scattering angle curve. These are indicative of orbiting collisions, where the interacting particles rotate around their CoM. The orbiting phenomenon is typically observed during collisions occurring at low ε_{tr}

in the presence of an attractive interaction potential, when ε_{tr} nearly equals the sum of the static potential from the PES [$\varphi_{cid}(r)$ in this case] and the centrifugal potential given by $\varepsilon_{tr}b^2/r^2$, and when $\varphi_{cid}(r) + \varepsilon_{tr}b^2/r^2$ is at a maximum. The scattering angle curves at the exact instances of orbiting exhibit discontinuities. Points with large negative scattering angles represent collisions where the incoming atom spirals around the molecule and eventually gets scattered away. Such orbiting complexes are a likely intermediary in the recombination process resulting in molecules [92–95].

Maximum instances of orbiting are observed for collisions that take place along $1^1A'$, $1^1A''$, $1^3A'$, and $1^3A''$ surfaces for b between 2.5 and 4.5 Å, as seen in Figs. 4(a), 4(c), 4(d), and 4(f). This is likely due to more attractive regions in the interaction potential present on these surfaces, compared to the other PESs in the set generated by Varga *et al.* [54]. Further, the exact impact parameters at which the orbiting occurs depends on the vibrational state of the O₂. In general, more orbiting instances are observed when the molecule is vibrationally excited owing to the increased attractive nature of the underlying potential as discussed in Sec. IV A. In case of the remaining five surfaces, most of the interaction potential is repulsive. However, for all three quintet surfaces, undulations in the StS potentials around ~ 2 to 3.5 Å when O₂ is vibrationally excited create shallow attractive wells in the interaction potential, which leads to orbiting around the 2.5 to 4.5 Å impact parameter range. For similar impact parameters, interactions involving O₂ on lower vibrational levels manifest as milder scattering with negative values for χ . Unlike the $1^1A'$, $1^1A''$, $1^3A'$, and $1^3A''$, the scattering angles along the $2^1A'$, $2^3A'$ surfaces appear to be only weakly dependent on the vibrational state of the O₂ molecule.

In summary, it is evident from Fig. 4 that the O + O₂ surfaces of varying spin states, whether ground or excited surfaces, exhibit different scattering angle profiles. Further, these profiles have a dependence on the vibrational excitation of O₂, owing to the increasing tendency of attractive interactions occurring at increased vibrational levels. A number of orbiting interactions were also observed for low relative translational energy collisions, especially along the ground and second excited singlet and triplet surfaces. In the subsequent sections we explore the influence of these scattering angles on the StS collision integrals, computed along each surface.

C. State-based collision integrals

Based on the scattering angles provided in Sec. IV B, the diffusion collision integrals as a function of temperature are evaluated using Eq. (3) and (4), by setting s and t to 1. The state-based transport cross section [Eq. (3)] plots as a function of relative translational energy, ε_{tr} , are shown in Sec. 2 of the Supplemental Material [90]. It should also be noted that while the collision integrals are presented here up to 30 000 K, for temperatures exceeding ~ 20 000 K, electronic excitation is likely to become important. This would give rise to additional collision pathways which have been neglected in the present calculation due to the lack of availability of suitable PESs. Thus, it is expected that the collision integrals presented here are most accurate up to ~ 20 000 K.

Figure 5 shows the vibrational state-based diffusion $\sigma^2\Omega^{(1,1)*}$ collision integrals normalized based on the hard-sphere factor, as a function of temperature, T , for the nine Varga *et al.* [54] PESs. As described earlier, the curves in each plot represent interactions with different vibrational levels of the O₂ molecule. The StS collision integrals are computed up to a temperature of 30 000 K, and an inset is provided for each surface in Fig. 5 to better indicate the variations in $\sigma^2\Omega^{(1,1)*}$ for temperatures less than 6000 K. The state-based $\sigma^2\Omega^{(1,1)*}$ results presented here are averaged over all possible interaction orientations defined by the angle, θ [Fig. 1, Eq. (6)]. It can be seen from Fig. 5 that the StS diffusion collision integral values depend on the underlying surface and the vibrational excitation of O₂. As expected the StS collision integrals are a decreasing function of T . Similar results for the StS viscosity collision integrals are provided in Sec. 3 of the Supplemental Material [90].

Collision integrals for diffusion for the $1^1A'$, $1^1A''$, $1^3A'$, and $1^3A''$ surfaces shown in Figs. 5(a), 5(c), 5(d), and 5(f) exhibit similar variations in values with vibrational excitation of O₂. These

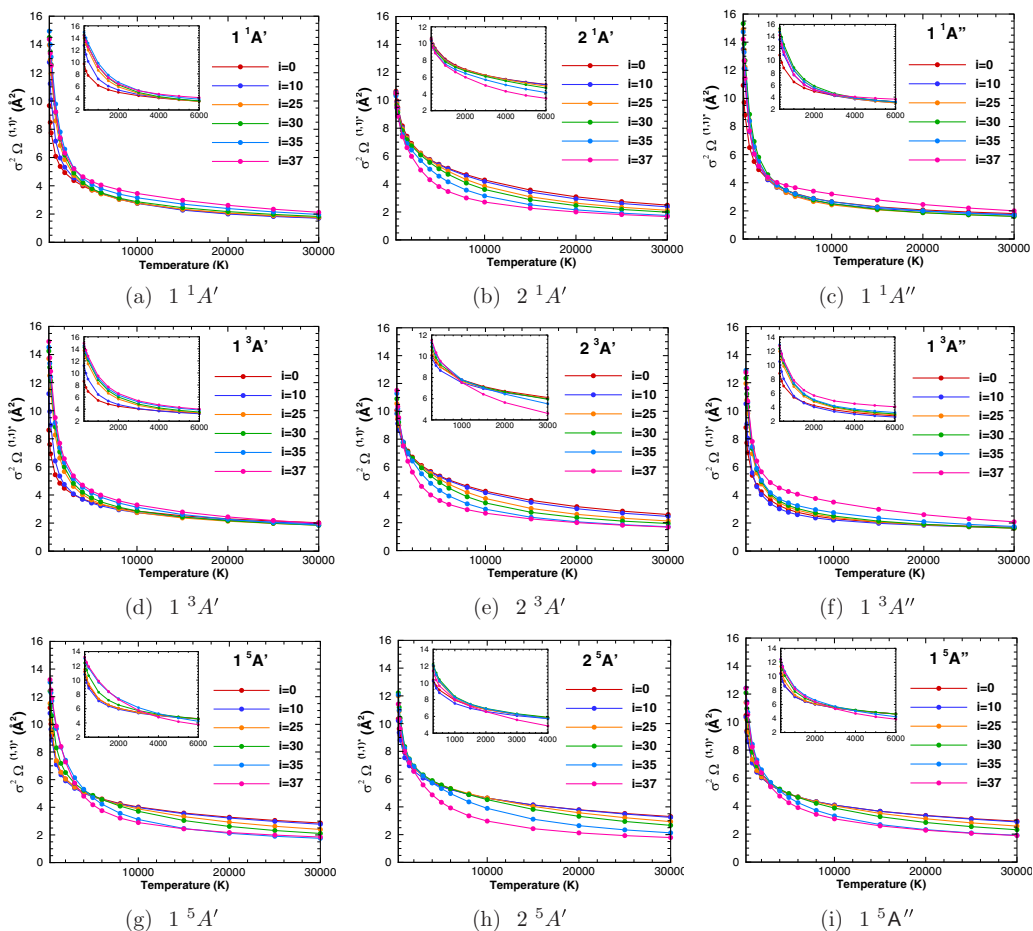


FIG. 5. Orientation-averaged state-based $\sigma^2\Omega^{(1,1)*}$ collision integrals vs temperature, for six vibrational levels of O_2 . Panels (a)–(c) correspond to the singlet state, (d)–(f) the triplet surfaces, and (g)–(i) the quintet surfaces. The insets show variation in StS $\sigma^2\Omega^{(1,1)*}$ values at $T < 6000$ K.

surfaces indicate that the $\sigma^2\Omega^{(1,1)*}$ values increase with vibrational excitation of the O_2 molecule at high temperatures, which can be attributed to the deepening attractive well in the StS potential for higher vibrational states of O_2 [Figs. 3(a), 3(c), 3(d), and 3(f)]. Deviation from this trend is observed in Fig. 5(c) for the $1^1A'$ and $1^1A''$ surfaces when $T < 3000$ K as highlighted in the insets. At these temperatures, interactions with O_2 in $i = 35$ and $i = 30$ lead to the highest values in $\sigma^2\Omega^{(1,1)*}$ for the $1^1A'$ and $1^1A''$ surfaces, respectively. This nonmonotonic behavior in the collision integral values at $T < 3000$ K is likely due to the long-range portion of the StS potential curves (~ 2.5 – 4.5 Å) where a monotonic/uniform dependence on the vibrational state of the molecule was not observed. It should also be noted that maximum variation in the StS $\sigma^2\Omega^{(1,1)*}$ values with vibrational level of O_2 persists only up to $T \approx 6000$ – 7000 K for the $1^1A'$ and $1^1A''$ surface. For the triplet surfaces, this temperature is around 10000 K. However, along all four surfaces over the entire temperature range considered, the $\sigma^2\Omega^{(1,1)*}$ values corresponding to higher vibrational levels, namely, $i = 35$ and 37 , are considerably higher than those corresponding to the other vibrational levels of O_2 , which nearly collapse on a single curve.

Unlike the four singlet and triplet surfaces discussed above, Figs. 5(g) to 5(i) corresponding to collisions occurring on the quintet, $1^5A'$, $2^5A'$, $1^5A''$, and the first excited singlet and triplet,

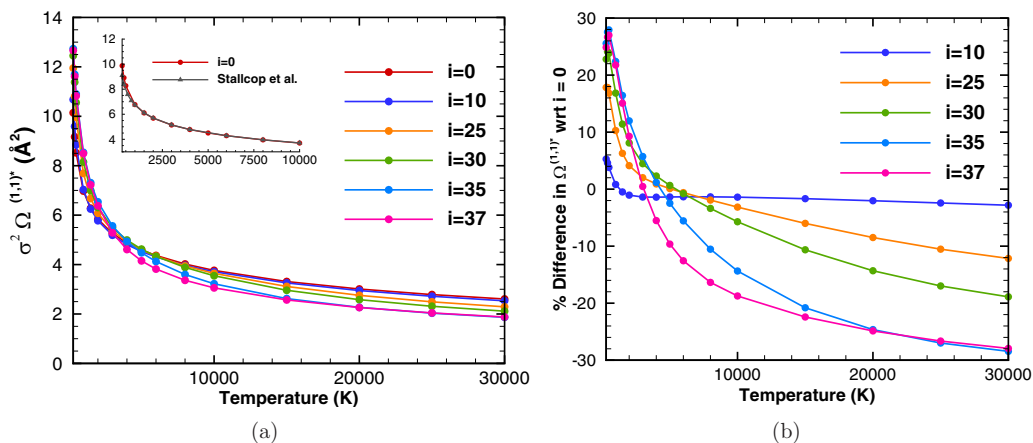


FIG. 6. (a) Degeneracy-weighted surface-averaged $\sigma^2 \Omega^{(1,1)*}$ collision integrals based on the nine Varga *et al.* [54] PESs, with collision integrals for each surface obtained by averaging over all possible orientations. Inset in (a) compares the degeneracy-weighted surface-averaged collision integrals for O_2 on $i = 0$ computed in the present work, and the $O + O_2$ collision integrals from Stallcop *et al.* [84], both calculations performed at a relative orientation of $\theta = 54.74^\circ$ between O and the CoM O_2 . (b) Percentage difference in surface-averaged $\sigma^2 \Omega^{(1,1)*}$ values for excited O_2 , with respect to O_2 present on ground state, $i = 0$.

$2^1A'$, $2^3A'$ surfaces indicate that most variation in the StS $\sigma^2 \Omega^{(1,1)*}$ values arise for $T \gtrsim 5000$ K. Furthermore, for these temperatures, there is a monotonic decrease in the StS $\sigma^2 \Omega^{(1,1)*}$ with vibrational excitation of O_2 , contrasting the increase in the collision integral value with vibrational level that was observed along the $1^1A'$, $1^1A''$, $1^3A'$, and $1^3A''$ surfaces. This decrease in collision integral values can be linked to the nature of the StS potential along the quintet surfaces, as shown in Figs. 3(g) to 3(i). For collisions occurring at low temperatures (on average, low ε_{tr}), the incoming atom encounters a potential barrier around $r \sim 2.5$ \AA , irrespective of the vibrational state of O_2 . However, the height of this barrier decreases with vibrational excitation of O_2 , and therefore, as the value of temperature (on average, ε_{tr}) increases, incoming atoms interacting with vibrationally excited O_2 are able to cross the repulsive barrier around $r \sim 2$ \AA and approach much closer to the CoM of the molecule before getting repelled. This contribution from a different region of the StS potential curve occurring at relatively short interatomic distances, resulting in the molecule appearing “smaller,” likely leads to the observed decrease in collision integral values with vibrational excitation. It can, however, be observed from the insets provided for the quintet surfaces in Figs. 5(g) to 5(i) that for temperatures up to ~ 5000 K, the state-based $\sigma^2 \Omega^{(1,1)*}$ values nearly increase (although not monotonically) as the interacting O_2 becomes more vibrationally excited. Similar to the singlet and triplet surface, this can be attributed to the shallow wells present in the long-range portion of the interacting StS potential. It should be noted that calculations for the $\sigma^2 \Omega^{(2,2)*}$ viscosity collision integrals from all nine surfaces are provided in Fig. 4 of the Supplemental Material [90].

Next, a degeneracy-weighted average of the diffusion collision integral values from all nine surfaces is computed for each vibrational level of O_2 and presented in Fig. 6(a). Since the highest degeneracy (5/27) is associated with each of the quintet surfaces where the StS $\sigma^2 \Omega^{(1,1)*}$ values exhibit the largest dependence on the vibrational state of O_2 for $T \gtrsim 5000$ K, a similar trend is revealed by the “surface-averaged” StS collision integrals based on all nine surfaces. Figure 6(b) indicates the percentage difference between the collision integral values corresponding to O_2 present on excited vibrational states, with respect to the ground-state value. Not surprisingly, this difference increases for higher vibrational levels. Furthermore, up to $T \sim 6000$ K the excited vibrational state collision integral values are, in general, higher than those corresponding to ground state, while at

higher temperatures, this trend reverses with the collision integral value decreasing with vibrational excitation of O_2 . The differences between collision integrals for O_2 present on $i = 37$ and $i = 0$ take values as high as 30% at both ends of the temperature range considered. Similar findings were obtained for the state-based, surface-averaged viscosity collision, and these are provided in Fig. 5 of the Supplemental Material [90].

The inset shown in Fig. 6(a) compares the surface-averaged $\sigma^2\Omega^{(1,1)*}$ value as a function of T for ground-state O_2 , with those calculated by Stallcop *et al.* [84] for the $O + O_2$ system, also in the ground vibrational state. The calculation performed by Stallcop *et al.* [84] accounted for all nine PESs along which the $O + O_2$ interaction occurs and was computed for a relative orientation of $\theta = 54.74^\circ$ between O and the CoM of O_2 . It can be seen that there is an excellent agreement between the present work and those computed by Stallcop *et al.* [84]. Additionally, it must be noted that Stallcop *et al.* [84] obtained the transport cross sections using the quantum mechanical sudden approximation method and have previously obtained good agreement between their sudden approximation calculation of collision integrals with close-coupling quantum scattering calculations [96]. Thus, the agreement of the *classical* calculation of transport collision integrals of this work with those of Stallcop *et al.* [84] highlights that such classical calculations are sufficient to capture transport collisional properties of the $O + O_2$ system.

To summarize, it was found that the nature of the PES governing the interaction between O and O_2 influences how the molecule's vibrational excitation impacts the values of $\sigma^2\Omega^{(1,1)*}$ and $\sigma^2\Omega^{(2,2)*}$ collision integrals. For surfaces that in general presented increasingly attractive StS potential curves with vibrational excitation of O_2 , the collision integral values were found to increase as the interacting molecule is vibrationally excited. In surfaces where an attractive well manifests only at higher vibrational levels, e.g., the $1^5A'$, $1^5A''$ surface [Figs. 3(g) and 3(i)], collision integral values decreased with vibrational excitation of O_2 for a high-temperature condition. The surface-averaged vibrational state-based $\sigma^2\Omega^{(1,1)*}$ values typically increase with vibrational excitation of O_2 for T up to ~ 6000 K, and then decrease at higher temperatures similar to the highest statistical weight quintet surfaces. It should also be noted that similar nonmonotonic variation of collision integral values with vibrational excitation has been observed by Han *et al.* [72] for the $N_2 + O$ system. Finally, these surface-averaged vibrational state-based $O + O_2$ diffusion and viscosity collision integrals as a function of T have been fitted to the Gupta-Yos form [97] for each vibrational level. The form of these fits and the coefficients are tabulated in the Appendix for use in state-based CFD codes. The StS collision integral data for each vibrational level used to perform these fits are provided in Tables 2 to 4 of the Supplemental Material [90].

V. DISCUSSION

In Sec. VA the state-based potentials and collision integrals obtained from the Varga *et al.* [54] surfaces are compared with the ones obtained from the Varandas and Pais [49] PES. Although a similar comparison was performed in our previous study [98], it was restricted to a single orientation angle and lower range of temperatures. Next, the vibrational state-based collision integrals computed in this work are compared with empirical models for obtaining excited vibrational level collision integrals in Sec. VB. "State-averaged" collision integrals under equilibrium and two-temperature conditions are presented in Sec. VC, and state-based viscosity and translational thermal conductivity values under equilibrium conditions are presented in Sec. VD.

A. Comparison with Varandas and Pais PES

Here we perform a direct comparison of the state-based potentials and the $\sigma^2\Omega^{(1,1)*}$ collision integrals for the Varga *et al.* [54] and Varandas and Pais [49] PES. Since the Varandas and Pais [49] surface provides only a single, ground-state PES, the results from this PES are compared to those obtained from the $1^1A'$ surface by Varga *et al.* [54] Further, as the underlying two-body O_2 potential is different for both these surfaces, the number of vibrational levels and their corresponding energies

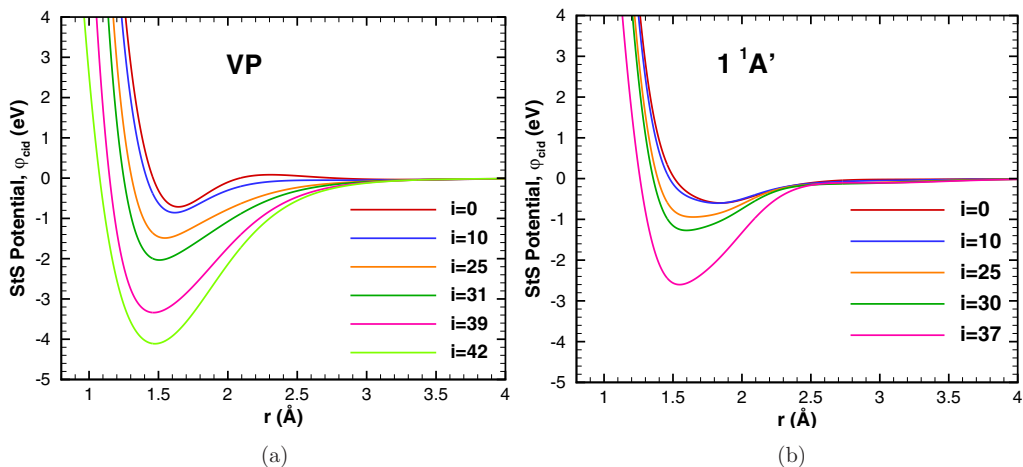


FIG. 7. State-based potential curves when the O atom approaches the CoM of O_2 present at different vibrational levels, i . (a) Varandas and Pais [49] surface; (b) $1^1A'$ surface from Varga *et al.* [54].

are different. Hence, five vibrational levels are chosen for the Varandas and Pais [49] and the Varga *et al.* [54] surfaces, such that their energies are nearly equal, even if the actual vibrational quantum numbers have different values. For the $1^1A'$ surface by Varga *et al.* [54], the chosen vibrational levels are 0, 10, 25, 30, and 37, and the corresponding vibrational levels from the Varandas and Pais [49] PES are 0, 10, 25, 31, and 39. Since the Varandas and Pais [49] surface allows up to $i = 47$ vibrational levels with zero rotation [47], an additional level, $i = 42$, is considered for this surface.

1. State-based potentials

Figure 7 shows the vibrational state-based potentials from the two surfaces under study, for an orientation angle, $\theta = 54.74^\circ$, as a function of r , which is the distance of the approaching O atom from the CoM of the O_2 molecule. A clear difference can be observed in the StS potentials computed from both these surfaces. While both sets of surfaces indicate a variation in the interaction potential with vibrational state of the molecule, a more pronounced influence is reflected in the Varandas and Pais [49] surface. Further, as vibrational excitation increases, deeper wells are produced in the Varandas and Pais [49] surface than by the $1^1A'$ surface by Varga *et al.* [54]. The value of the maximum well depth in the Varandas and Pais [49] surface is around 4 eV, whereas the $1^1A'$ surface by Varga *et al.* [54] indicated a well depth of ~ 2.5 eV. These differences are likely due to the different variations of well depth with the orientation angle, θ , for these two PESs. However, the repulsive portion of the StS potential at low r appears to be similar in surfaces.

2. Collision integrals

The vibrational state-based $\sigma^2\Omega^{(1,1)*}$ collision integrals computed by averaging over orientations are compared in Fig. 8. The surface-averaged diffusion collision integrals considering all nine surfaces by Varga *et al.* [54] are presented here [Fig. 8(c)] again for ease of comparison. Figure 8 reveals that the state-based diffusion collision integral computed from the Varandas and Pais [49] surface exhibits a more pronounced dependence on the vibrational state of the O_2 than those computed from the $1^1A'$ surface by Varga *et al.* [54]. Additionally, Figs. 8(a) and 8(b) indicate a higher value for the StS diffusion collision integrals from the Varandas and Pais [49] PES, with the influence of vibrational excitation of O_2 on the $\sigma^2\Omega^{(1,1)*}$ integrals evident over the entire temperature range considered, unlike the StS collision integrals from the $1^1A'$ surface

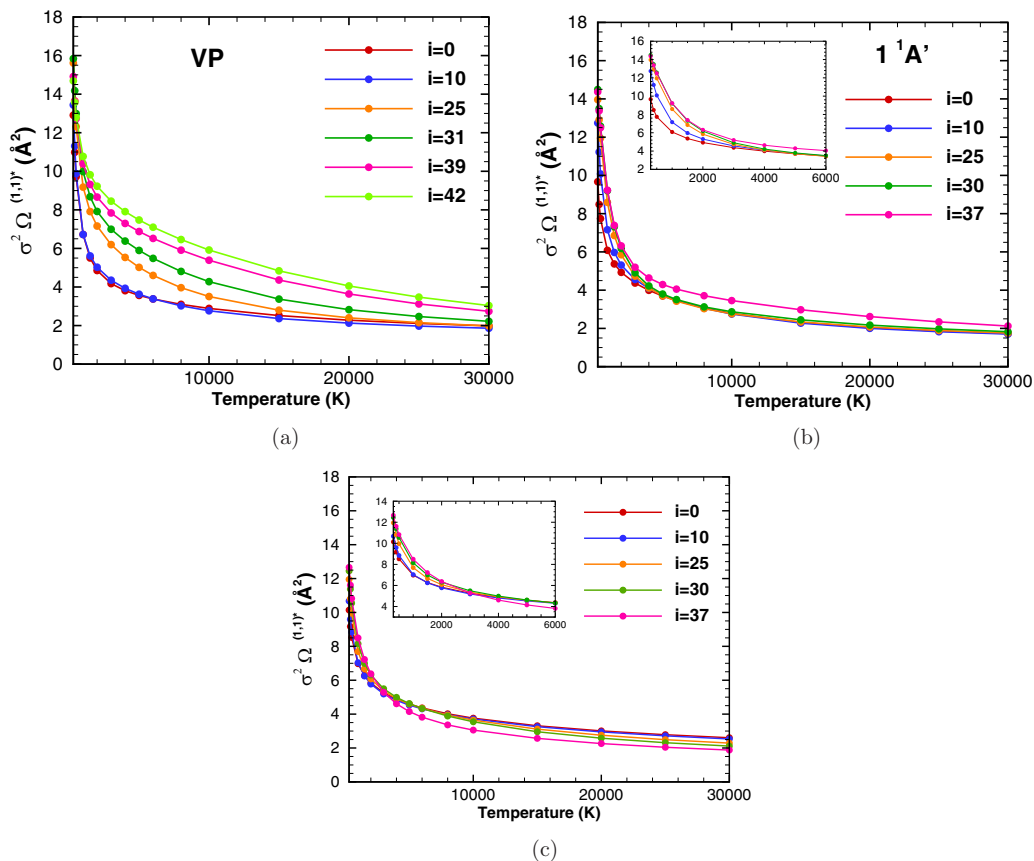


FIG. 8. State-based $\sigma^2 \Omega^{(1,1)*}$ for the O + O₂ system averaged over orientations, as a function of temperature, with O₂ present on different vibrational levels, i . (a) Varandas and Pais [49] surface; (b) $1^1A'$ surface from Varga *et al.*; (c) surface-averaged collision integral from all nine Varga *et al.* [54] surfaces. The insets are provided to better highlight the variation in the StS $\sigma^2 \Omega^{(1,1)*}$ values for T up to 6000 K.

that do not exhibit such a strong dependence on the vibrational state of O₂ at high temperature values.

The surface-averaged diffusion collision integrals accounting for all nine Varga *et al.* [54] surfaces are presented in Fig. 8(c). It can be seen that the dependence of these surface-averaged collision integral on the vibrational state of O₂ is considerably different from the Varandas and Pais [49] surface, shown in Fig. 8(a). While the Varandas and Pais [49] collision integrals vary significantly with the molecule's vibrational state over the entire temperature range, the surface-averaged $\sigma^2 \Omega^{(1,1)*}$ collision integrals show a relatively lower variation with vibrational level. Additionally, at high temperatures, the value of the $i = 37$ surface-averaged $\sigma^2 \Omega^{(1,1)*}$ integral is much lower than those corresponding to other vibrational states. Again, this trend is not captured by the Varandas and Pais [49] surface as it accounts only for the interactions along the ground-state singlet surface, and neglects the higher spin and excited surfaces for each spin state which are responsible for the decrease in the diffusion collision integral values for vibrationally excited molecules at high temperatures.

B. Comparison with empirical models

Here we compare the vibrational state-based collision integrals computed rigorously from the Varga *et al.* [54] and the Varandas and Pais [49] surfaces to an empirical model proposed by Kustova *et al.* [70]. The necessity for such an empirical model has been a lack of availability of rigorously computed StS transport collision data. In this model by Kustova *et al.*, collision integrals for excited vibrational levels are assumed to be proportional to the ground vibrational state collision integral values according to

$$\Omega_{cidk}^{\text{model},(s,t)} = \frac{d_{ci,dk}^2}{d_{c0,d0}^2} \Omega_{c0d0}^{(s,t)} \quad (7)$$

where Ω_{c0d0} is the ground vibrational state collision integral, and $d_{ci,dk}$ represents the diameter computed as

$$d_{ci,dk} = \frac{d_{ci} + d_{dk}}{2}. \quad (8)$$

The surface-averaged, state-based diffusion collision integral values for O₂ on vibrational states 10, 25, 30, and 37 computed directly from the PES in the present work [Fig. 6(a)] are compared against those predicted by Eq. (7) in Fig. 9. It should also be noted that all comparisons are done for collision integral values normalized by the hard-sphere factor [80,84]. The diameter of O₂ at each vibrational level required in Eq. (8) is taken to be the average bond length that is used to directly compute the StS collision integral values from the PES.

Figures 9(a) and 9(b) represent the surface-averaged StS $\sigma^2 \Omega^{(1,1)*}$ values computed in the present work from the nine surfaces by Varga *et al.* [54] compared with the ones obtained from the model by Kustova *et al.* in Eq. (7), and the percentage difference in the collision integral values with respect to the calculations in the present work, respectively. The same quantities are computed from the Varandas and Pais [49] surface in Figs. 9(c) and 9(d). It is clear from Figs. 9(a) and 9(c) that for both sets of surfaces considered, a significant difference exists between the StS collision integrals predicted by the empirical model and those computed directly from the PES, with differences increasing with vibrational excitation of O₂. Specifically, the surface-averaged $\sigma^2 \Omega^{(1,1)*}$ on $i = 37$ from the Varga *et al.* [54] surfaces and the empirical model shows a discrepancy of around 80%. Furthermore, since the diameter employed in Eq. (7) increases with vibrational excitation of the molecule, the model always predicts an increase in the state-based collision integral values when O₂ is excited to a higher vibrational level. However, the surface-averaged $\sigma^2 \Omega^{(1,1)*}$ values computed from the Varga *et al.* [54] set of surfaces decrease with vibrational excitation of O₂ for $T \gtrsim 6000$ K as discussed in detail in Sec. IV C, which the model in Eq. (7) is unable to account for. On the other hand, the increasingly attractive nature of the StS potential with vibrational excitation of O₂ from the Varandas and Pais [49] surface leads to a monotonic increase in the state-based $\sigma^2 \Omega^{(1,1)*}$ which the empirical model is able to correctly predict. Although the model qualitatively captures the influence of vibrational excitation on the StS collision integrals, errors around 35% are obtained between the model prediction and the StS $\sigma^2 \Omega^{(1,1)*}$ values computed directly from the PES.

C. State-averaged collision integrals

Based on the surface-averaged, state-based $\sigma^2 \Omega^{(1,1)*}$ values computed in this work by averaging over all nine surfaces by Varga *et al.* [54], vibrationally averaged $\sigma^2 \Omega^{(1,1)*}$ values are calculated for a two-temperature model, where T denotes the translational temperature, and the vibrational mode is described by a Boltzmann distribution at vibrational temperature, T_{vib} . The vibrationally averaged O + O₂ collision integral values are also evaluated for the equilibrium condition where $T = T_{\text{vib}}$, and then compared with those calculated by Stallcop *et al.* [84] for interactions involving ground-state O₂. It can be seen from Fig. 10(a) that for equilibrium conditions, there is a good agreement between the vibrationally averaged values under equilibrium conditions (red curve) and

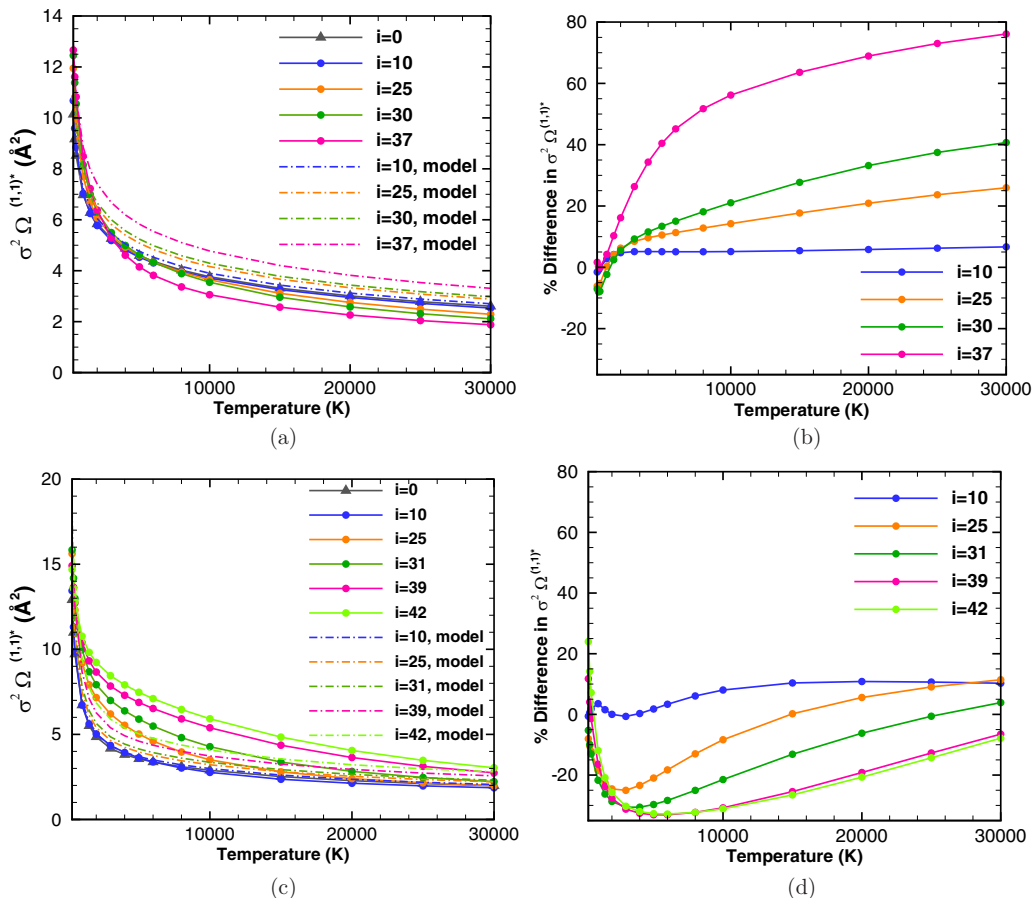


FIG. 9. Comparison between the state-based $\sigma^2 \Omega^{(1,1)*}$ values computed directly from the PES in the present work and those obtained by the empirical model proposed by Kustova *et al.* [Eqs. (7) and (8)] for (a) surface-averaged Varga *et al.* [54] surfaces; (c) Varandas and Pais [49] surface. Percentage difference between the two estimates for the StS $\sigma^2 \Omega^{(1,1)*}$ values with respect to the values calculated directly from the PES: (b) surface-averaged Varga *et al.* [54] surfaces; (d) Varandas and Pais [49] surface.

those computed by Stallcop *et al.* [84] (gray). Thus, it appears that even $\sim 30\%$ difference in the excited state collision integral values with respect to ground state [Fig. 6(b)] does not influence the vibrationally averaged result under equilibrium conditions.

Figure 10(a) also shows the two-temperature vibrationally averaged collision integral values as a function of T_{vib} , where each curve denotes a constant T , while in Fig. 10(b), percentage differences between the two-temperature and equilibrium $\sigma^2 \Omega^{(1,1)*}$ values are provided. While not much change is observed in vibrationally averaged $\sigma^2 \Omega^{(1,1)*}$ values as a function of T_{vib} , for $T = 5000$ and $10\,000$ K, for translational temperatures outside this range the vibrationally averaged collision integrals vary as a function of T_{vib} . For $T = 300, 500, \text{ and } 1000$ K when $T_{\text{vib}} \gg T$, the vibrationally averaged $\sigma^2 \Omega^{(1,1)*}$ values differ from the corresponding equilibrium values up to $\sim 10\%$. On the other hand, for $T = 20\,000$ and $30\,000$ K and low T_{vib} , differences up to $\sim 6\%$ are observed in the vibrationally averaged $\sigma^2 \Omega^{(1,1)*}$ values, with respect to the equilibrium case. Thus, for a translationally cool and vibrationally hot gas, or for a translationally hot and vibrationally cool gas, the two-temperature vibrationally averaged collision integrals values differ significantly from the equilibrium ones.

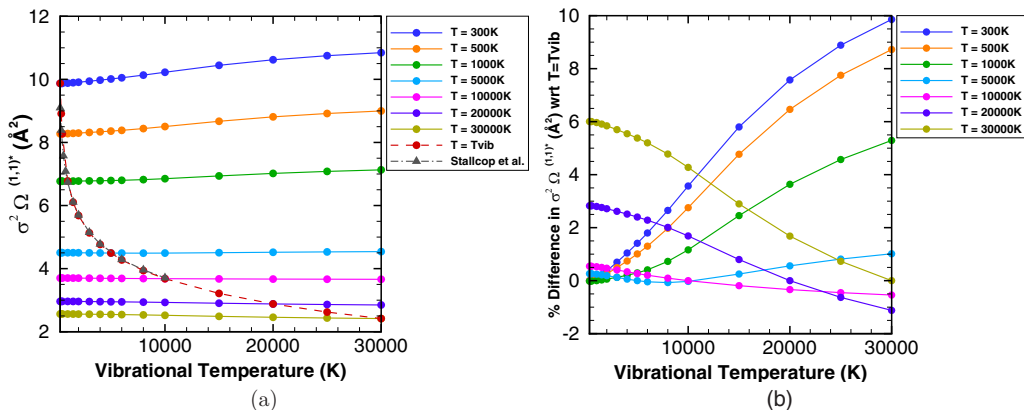


FIG. 10. (a) Vibrationally averaged $\sigma^2 \Omega^{(1,1)*}$ values based on a two-temperature model, plotted as a function of vibrational temperature, T_{vib} . Each curve corresponds to a fixed translational temperature, T . (b) Percentage difference between $\sigma^2 \Omega^{(1,1)*}$ values with respect to the values at equilibrium, defined at $T = T_{\text{vib}}$.

It should, however, be noted that this assessment assumes an equilibrium Boltzmann distribution within the vibrational mode and neglects the effect of molecular rotation. Understanding and quantifying these influences on state-resolved transport collision integrals are crucial for developing high-fidelity models for hypersonic reentry applications and shall be therefore be addressed in future efforts.

D. State-based transport coefficients under equilibrium

As a final study, the state-based translational thermal conductivity, λ_{tr} , and viscosity, μ , are computed for an $\text{O} + \text{O}_2$ mixture using the collision integrals calculated in this work from the nine *ab initio* surfaces by Varga *et al.* [54] These calculations are performed based on the Chapman-Enskog theory [99], under equilibrium conditions over a temperature range of 1000–15 000 K at a constant pressure of 1000 Pa. The mole fractions of the O and O_2 used in this calculation are shown as a function of T in Fig. 11. It should be noted that the vibrational states of O_2 are populated using

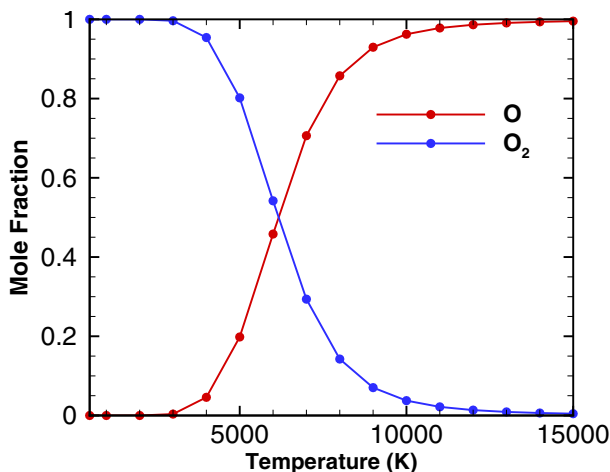


FIG. 11. Mole fraction of the $\text{O} + \text{O}_2$ mixture as a function of temperature at 1000 Pa.

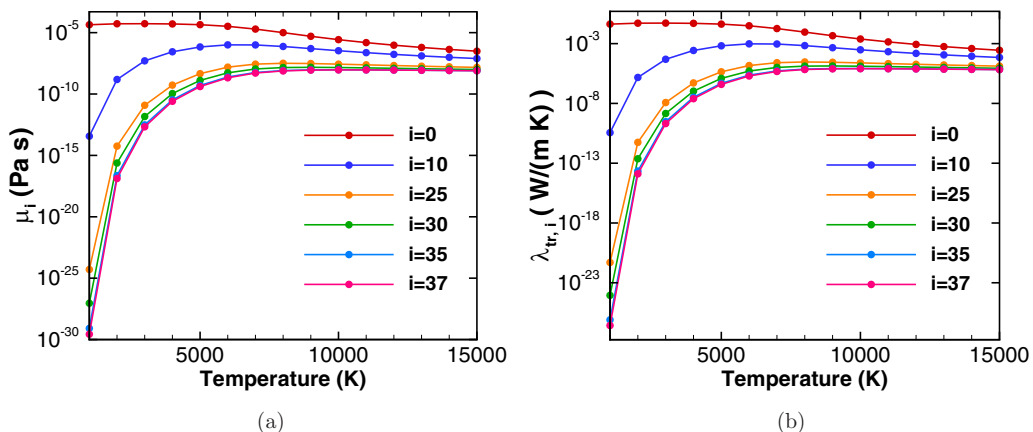


FIG. 12. State-based (a) viscosity and (b) translational thermal conductivity of vibrationally excited O_2 as a function of temperature, under equilibrium at 1000 Pa pressure.

the equilibrium Boltzmann distribution at temperature T . Since vibrational state-based collision integrals are available only for $O + O_2$ interactions, the $O_2 + O_2$ interactions are described using the collision integrals found in Bzowski *et al.* [100], and the $O + O$ collision integrals are obtained from Levin *et al.* [83].

Figure 12 shows the contribution of O_2 in vibrational levels, $i = 0, 10, 25, 30, 35, 37$, to the mixture viscosity and translational thermal conductivity. It is clear from Fig. 12 that the both viscosity and translational thermal conductivity are influenced by the vibrational excitation of O_2 . Although contributions from highly excited levels are negligible at $T \sim 1000$ K, the viscosity and translational thermal conductivity values of vibrationally excited O_2 increase with increasing temperature. Similar studies shall be carried out as part of future work, for a nonequilibrium flowfield, along with state-based $O_2 + O_2$ transport in order to better quantify the effect of employing a state-resolved oxygen system for hypersonic flow simulations.

VI. CONCLUSIONS

Collision dynamics principles have been extended in the present work to the state-based formulation, and a methodology is presented for calculating vibrationally resolved transport collisional properties, namely, scattering angles, cross sections, and collision integrals, from *ab initio* PESs. Based on the Varga *et al.* [54] set of surfaces, it was found that the state-based potentials depend on the spin and spatial degeneracy of the underlying PES. The $1^1A'$, $1^1A''$, $1^3A'$, and $1^3A''$ surfaces exhibited attractive state-based potentials, with the depth of the potential well increasing with vibrational excitation of the molecule. Consequently, these surfaces gave rise to more attractive scattering and instances of orbiting collisions for interactions that occurred at low values of relative translational energy. Additionally, for these surfaces, the state-based $\sigma^2 \Omega^{(1,1)*}$ collision integrals at temperatures greater than 6000 K exhibited a monotonic increase with vibrational excitation of the O_2 molecule. In the case of the remaining five surfaces, namely, the three quintet, the first excited singlet, and triplet surface, a steep repulsive potential barrier was observed in the StS potentials, with the barrier height decreasing with increase in the vibrational state of the molecule. Only for highly vibrationally excited O_2 , behind this small repulsive barrier, a region with an attractive well was found. Therefore, along these five surfaces for $T \gtrsim 3000$ K, the collision integrals corresponding to vibrationally excited O_2 decreased, compared to collisions involving O_2 present on lower vibrational states. Since the onset of a strong repulsive barrier at for O_2 present on higher vibrational levels occurred at much lower interatomic distances, these vibrationally excited molecules appeared “smaller” to the incoming atom giving rise to lower collision integral values. A degeneracy-weighted

average of the StS collision integrals over all nine Varga *et al.* [54] surfaces was computed to determine the “surface-averaged” StS $\sigma^2\Omega^{(1,1)*}$ values for a vibrationally resolved O + O₂ system. Additionally, very good agreement was obtained for the collision integrals of O interacting with ground-state O₂, between the present classical calculations and the quantum mechanical ones carried out by Stallcop *et al.* [84] (shown in the insets in Fig. 6 and Fig. 10) highlighting that such classical calculations are sufficient to capture transport collisional properties for the O + O₂ system.

A comparison of the transport collisional properties between the Varandas and Pais [49] surface and the 1¹A' surface by Varga *et al.* [54] revealed that the Varandas and Pais [49] surface exhibited more attractive StS potentials than the 1¹A' surface, which led to higher values for the state-based $\sigma^2\Omega^{(1,1)*}$ collision integral values. However, since the Varandas and Pais [49] surface does not account for the repulsive, high-spin states, it was unable to reproduce the monotonically decreasing trend in $\sigma^2\Omega^{(1,1)*}$ values with vibrational excitation for $T \gtrsim 6000$ K that was observed in the surface-averaged state-based collision integral values obtained from the nine Varga *et al.* [54] surfaces.

As a final step, the utility of the rigorously computed vibrational state-based collision integrals is demonstrated by comparing the present calculations with an empirical model proposed by Kustova *et al.*, where excited state collision integrals are computed by scaling the ground-state collision integral value by an average of diameter of the interacting species in their excited states. This empirical model was unable to capture the decrease in the surface-averaged $\sigma^2\Omega^{(1,1)*}$ values with vibrational excitation of O₂, at $T \gtrsim 6000$ K that was observed from calculations using the nine Varga *et al.* [54] surfaces, and differences as large as 80% were observed between the model values and the present calculation. When compared with the StS collision integral values obtained from the Varandas and Pais [49] surface which monotonically increase with vibrational excitation of O₂, the model prediction improved. However, differences around 35% were still obtained with respect to the present calculation. Thus, it was found that simplistic models such as the one tested in this study are unable to faithfully reproduce the influence of vibrational excitation on the StS collision integrals, since they do not account for the nontrivial dependence of the state-based potentials on the vibrational state of the interacting molecule, which in turn depend directly on the PES.

It was also found that under equilibrium conditions, the state-based viscosity and thermal conductivity are influenced by the vibrational excitation of O₂. Future efforts shall be directed towards incorporating effects of molecular rotation and extending this methodology to diatom-diatom systems, such as O₂ + O₂. This will allow for computing state-based transport properties such as mass diffusion coefficient, thermal conductivity, etc., for the complete oxygen system, based on which the impact of state-resolved transport models on heat flux calculations can be assessed for reentry applications.

ACKNOWLEDGMENTS

This work was supported by an Early Career Faculty grant from NASA’s Space Technology Research Grants Program, Grant No. NNX15AW46G, and the Air Force Office of Scientific Research under Award No. FA9550-17-1-0127. The authors acknowledge Dr. D. Schwenke from NASA Ames Research Center for many useful discussions and providing the energy eigenvalues and turning points for O₂ based on the Varga *et al.* surface. The authors also acknowledge Dr. E. Kustova from Saint Petersburg State University for the insightful discussion pertaining to the empirical collision integral model.

APPENDIX: STATE-BASED COLLISION INTEGRAL FITS

The surface-averaged vibrational state-based $\Omega^{(1,1)}$, $\Omega^{(1,2)}$, $\Omega^{(1,3)}$, and $\Omega^{(2,2)}$ collision integrals obtained by averaging over all nine surfaces proposed by Varga *et al.* [54] are evaluated at the effective orientation angle, $\theta = 54.74^\circ$, for interactions involving O₂ on vibrational states, $i = 0, 10, 15, 20, 25, 30, 32, 35,$ and 37 . For states that lie within these intervals, the collision integrals are

TABLE I. Fitting parameters for vibrational state-based $\pi\sigma^2\Omega^{(1,1)*}$ collision integrals in (\AA^2) for the O + O₂ system.

Vibrational state of O ₂	Energy (eV)	A	B	C	D
0	0.098	$-7.7222189 \times 10^{-3}$	1.8122316×10^{-1}	-1.6688572	4.8514156×10^3
1	0.292	$-7.9802637 \times 10^{-3}$	1.8814396×10^{-1}	-1.7311256	5.8444407×10^3
2	0.483	$-8.2319109 \times 10^{-3}$	1.9489316×10^{-1}	-1.7918596	7.0087696×10^3
3	0.671	$-8.4773657 \times 10^{-3}$	2.0147622×10^{-1}	-1.8511072	8.3680842×10^3
4	0.855	$-8.7168275 \times 10^{-3}$	2.0789846×10^{-1}	-1.9089155	9.9484483×10^3
5	1.036	$-8.9504901 \times 10^{-3}$	2.1416503×10^{-1}	-1.9653302	1.1778438×10^4
6	1.215	$-9.1785379 \times 10^{-3}$	2.2028086×10^{-1}	-2.0203946	1.3889239×10^4
7	1.390	$-9.4011468 \times 10^{-3}$	2.2625065×10^{-1}	-2.0741506	1.6314750×10^4
8	1.563	$-9.6184820 \times 10^{-3}$	2.3207880×10^{-1}	-2.1266369	1.9091643×10^4
9	1.732	$-9.8306962 \times 10^{-3}$	2.3776939×10^{-1}	-2.1778899	2.2259378×10^4
10	1.899	$-1.0037929 \times 10^{-2}$	2.4332617×10^{-1}	-2.2279425	2.5860192×10^4
11	2.063	$-1.0088412 \times 10^{-2}$	2.4410628×10^{-1}	-2.2332223	2.6446122×10^4
12	2.224	$-1.0139885 \times 10^{-2}$	2.4491295×10^{-1}	-2.2386734	2.7047747×10^4
13	2.383	$-1.0192269 \times 10^{-2}$	2.4574449×10^{-1}	-2.2442859	2.7665209×10^4
14	2.538	$-1.0245477 \times 10^{-2}$	2.4659916×10^{-1}	-2.2500494	2.8298564×10^4
15	2.691	$-1.0299424 \times 10^{-2}$	2.4747514×10^{-1}	-2.2559529	2.8947781×10^4
16	2.841	$-1.0606709 \times 10^{-2}$	2.5415493×10^{-1}	-2.3059266	3.3144968×10^4
17	2.988	$-1.0910142 \times 10^{-2}$	2.6074839×10^{-1}	-2.3551919	3.7865358×10^4
18	3.132	$-1.1209565 \times 10^{-2}$	2.6725243×10^{-1}	-2.4037310	4.3159634×10^4
19	3.273	$-1.1504787 \times 10^{-2}$	2.7366321×10^{-1}	-2.4515205	4.9080260×10^4
20	3.411	$-1.1795582 \times 10^{-2}$	2.7997616×10^{-1}	-2.4985309	5.5680666×10^4
21	3.546	$-1.2095351 \times 10^{-2}$	2.8604307×10^{-1}	-2.5412676	6.2431837×10^4
22	3.678	$-1.2396553 \times 10^{-2}$	2.9215918×10^{-1}	-2.5843830	7.0029440×10^4
23	3.807	$-1.2698324 \times 10^{-2}$	2.9830564×10^{-1}	-2.6277440	7.8558970×10^4
24	3.932	$-1.2999740 \times 10^{-2}$	3.0446236×10^{-1}	-2.6712082	8.8106593×10^4
25	4.053	$-1.3299806 \times 10^{-2}$	3.1060774×10^{-1}	-2.7146220	9.8755845×10^4
26	4.171	$-1.3386870 \times 10^{-2}$	3.1032636×10^{-1}	-2.6981911	9.2887631×10^4
27	4.284	$-1.3495053 \times 10^{-2}$	3.1061222×10^{-1}	-2.6865414	8.8463936×10^4
28	4.394	$-1.3621809 \times 10^{-2}$	3.1141067×10^{-1}	-2.6792859	8.5229831×10^4
29	4.499	$-1.3764389 \times 10^{-2}$	3.1266330×10^{-1}	-2.6760154	8.2988527×10^4
30	4.599	$-1.3919784 \times 10^{-2}$	3.1430698×10^{-1}	-2.6762928	8.1583939×10^4
31	4.693	$-1.3379265 \times 10^{-2}$	2.9788718×10^{-1}	-2.5260801	5.3525234×10^4
32	4.782	$-1.2906621 \times 10^{-2}$	2.8326006×10^{-1}	-2.3909292	3.6553948×10^4
33	4.865	$-1.0807823 \times 10^{-2}$	2.2989646×10^{-1}	-1.9568608	1.1794035×10^4
34	4.939	$-8.9022371 \times 10^{-3}$	1.8137952×10^{-1}	-1.5618638	4.2104242×10^3
35	5.005	$-7.2230749 \times 10^{-3}$	1.3857223×10^{-1}	-1.2130555	1.6945655×10^3
36	5.060	$-3.3875071 \times 10^{-4}$	$-1.6086083 \times 10^{-2}$	$-9.4109670 \times 10^{-2}$	1.2394235×10^2
37	5.099	4.8049659×10^{-3}	$-1.3175260 \times 10^{-1}$	7.4382978×10^{-1}	1.7421703×10^1

linearly interpolated based on the energy eigenvalue for each vibrational state. The surface-averaged state-based diffusion and viscosity collision integrals and B_{coll} given by

$$B_{\text{coll}} = \frac{5\Omega^{(1,2)} - \Omega^{(1,3)}}{5\Omega^{(1,1)}} \quad (\text{A1})$$

TABLE II. Fitting parameters for vibrational state-based $\pi\sigma^2\Omega^{(2,2)*}$ collision integrals in (\AA^2) for the O + O₂ system.

Vibrational state of O ₂	Energy (eV)	A	B	C	D
0	0.098	$-8.7753735 \times 10^{-3}$	2.0885231×10^{-1}	-1.8799206	8.9717728×10^3
1	0.292	$-9.0085823 \times 10^{-3}$	2.1548682×10^{-1}	-1.9422354	1.0859400×10^4
2	0.483	$-9.2357848 \times 10^{-3}$	2.2195609×10^{-1}	-2.0030457	1.3085153×10^4
3	0.671	$-9.4571709 \times 10^{-3}$	2.2826518×10^{-1}	-2.0623961	1.5698332×10^4
4	0.855	$-9.6729258 \times 10^{-3}$	2.3441904×10^{-1}	-2.1203302	1.8753632×10^4
5	1.036	$-9.8832296 \times 10^{-3}$	2.4042249×10^{-1}	-2.1768907	2.2311489×10^4
6	1.215	$-1.0088254 \times 10^{-2}$	2.4628013×10^{-1}	-2.2321185	2.6438375×10^4
7	1.390	$-1.0288165 \times 10^{-2}$	2.5199636×10^{-1}	-2.2860524	3.1207117×10^4
8	1.563	$-1.0483116 \times 10^{-2}$	2.5757533×10^{-1}	-2.3387294	3.6697113×10^4
9	1.732	$-1.0673251 \times 10^{-2}$	2.6302090×10^{-1}	-2.3901834	4.2994471×10^4
10	1.899	$-1.0858704 \times 10^{-2}$	2.6833659×10^{-1}	-2.4404457	5.0192096×10^4
11	2.063	$-1.0858024 \times 10^{-2}$	2.6803327×10^{-1}	-2.4380495	5.0377535×10^4
12	2.224	$-1.0858756 \times 10^{-2}$	2.6776524×10^{-1}	-2.4358896	5.0577573×10^4
13	2.383	$-1.0860831 \times 10^{-2}$	2.6753105×10^{-1}	-2.4339572	5.0791813×10^4
14	2.538	$-1.0864179 \times 10^{-2}$	2.6732925×10^{-1}	-2.4322436	5.1019825×10^4
15	2.691	$-1.0868732 \times 10^{-2}$	2.6715845×10^{-1}	-2.4307403	5.1261139×10^4
16	2.841	$-1.1298419 \times 10^{-2}$	2.7691219×10^{-1}	-2.5054071	6.2524381×10^4
17	2.988	$-1.1719896 \times 10^{-2}$	2.8647411×10^{-1}	-2.5785429	7.5934778×10^4
18	3.132	$-1.2133092 \times 10^{-2}$	2.9584309×10^{-1}	-2.6501441	9.1825978×10^4
19	3.273	$-1.2537895 \times 10^{-2}$	3.0501703×10^{-1}	-2.7201996	1.1056511×10^5
20	3.411	$-1.2934147 \times 10^{-2}$	3.1399280×10^{-1}	-2.7886901	1.3255102×10^5
21	3.546	$-1.3370331 \times 10^{-2}$	3.2339055×10^{-1}	-2.8576151	1.5884666×10^5
22	3.678	$-1.3804080 \times 10^{-2}$	3.3274550×10^{-1}	-2.9262127	1.9010060×10^5
23	3.807	$-1.4234435 \times 10^{-2}$	3.4203638×10^{-1}	-2.9943292	2.2711363×10^5
24	3.932	$-1.4660365 \times 10^{-2}$	3.5124030×10^{-1}	-3.0617991	2.7076168×10^5
25	4.053	$-1.5080752 \times 10^{-2}$	3.6033245×10^{-1}	-3.1284423	3.2198025×10^5
26	4.171	$-1.5472011 \times 10^{-2}$	3.6696876×10^{-1}	-3.1633147	3.4334222×10^5
27	4.284	$-1.5881906 \times 10^{-2}$	3.7412499×10^{-1}	-3.2026896	3.7050520×10^5
28	4.394	$-1.6306489 \times 10^{-2}$	3.8171341×10^{-1}	-3.2459260	4.0397791×10^5
29	4.499	$-1.6741441 \times 10^{-2}$	3.8963880×10^{-1}	-3.2923324	4.4431903×10^5
30	4.599	$-1.7181971 \times 10^{-2}$	3.9779629×10^{-1}	-3.3411529	4.9206221×10^5
31	4.693	$-1.7120619 \times 10^{-2}$	3.9152652×10^{-1}	-3.2604225	3.7711425×10^5
32	4.782	$-1.7123071 \times 10^{-2}$	3.8701374×10^{-1}	-3.1949605	3.0132960×10^5
33	4.865	$-1.5371968 \times 10^{-2}$	3.3951102×10^{-1}	-2.7883325	1.0007087×10^5
34	4.939	$-1.3820557 \times 10^{-2}$	2.9718461×10^{-1}	-2.4247085	3.7255857×10^4
35	5.005	$-1.2485484 \times 10^{-2}$	2.6055245×10^{-1}	-2.1088796	1.5762224×10^4
36	5.060	$-2.7995635 \times 10^{-3}$	3.6246992×10^{-2}	$-4.2722726 \times 10^{-1}$	2.6474075×10^2
37	5.099	4.4204477×10^{-3}	$-1.3097524 \times 10^{-1}$	8.2679268×10^{-1}	1.2550059×10^1

are nondimensionalized based on the corresponding hard-sphere values [80,84], and fit to the following functional forms:

$$\pi\sigma^2\Omega^{(s,t)*} = D T^{[A(\ln T)^2 + B \ln T + C]}, \quad (\text{A2})$$

$$B_{\text{coll}}^* = D T^{[A(\ln T)^2 + B \ln T + C]}. \quad (\text{A3})$$

TABLE III. Fitting parameters for vibrational state-based B_{coll}^* for the O + O₂ system.

Vibrational state of O ₂	Energy (eV)	A	B	C	D
0	0.098	$-2.0344515 \times 10^{-3}$	5.6717768×10^{-2}	$-4.9551863 \times 10^{-1}$	4.5563232
1	0.292	$-2.0465392 \times 10^{-3}$	5.7513748×10^{-2}	$-5.0621601 \times 10^{-1}$	4.7457804
2	0.483	$-2.0566607 \times 10^{-3}$	5.8249931×10^{-2}	$-5.1632593 \times 10^{-1}$	4.9338410
3	0.671	$-2.0649505 \times 10^{-3}$	5.8929994×10^{-2}	$-5.2588170 \times 10^{-1}$	5.1202414
4	0.855	$-2.0715337 \times 10^{-3}$	5.9557380×10^{-2}	$-5.3491462 \times 10^{-1}$	5.3047434
5	1.036	$-2.0765272 \times 10^{-3}$	6.0135311×10^{-2}	$-5.4345408 \times 10^{-1}$	5.4871327
6	1.215	$-2.0800399 \times 10^{-3}$	6.0666795×10^{-2}	$-5.5152755 \times 10^{-1}$	5.6672154
7	1.390	$-2.0821735 \times 10^{-3}$	6.1154647×10^{-2}	$-5.5916075 \times 10^{-1}$	5.8448171
8	1.563	$-2.0830228 \times 10^{-3}$	6.1601491×10^{-2}	$-5.6637770 \times 10^{-1}$	6.0197798
9	1.732	$-2.0826768 \times 10^{-3}$	6.2009779×10^{-2}	$-5.7320077 \times 10^{-1}$	6.1919594
10	1.899	$-2.0812186 \times 10^{-3}$	6.2381799×10^{-2}	$-5.7965079 \times 10^{-1}$	6.3612239
11	2.063	$-2.1985971 \times 10^{-3}$	6.5271615×10^{-2}	$-6.0272805 \times 10^{-1}$	6.7616126
12	2.224	$-2.3122580 \times 10^{-3}$	6.8071821×10^{-2}	$-6.2509594 \times 10^{-1}$	7.1737298
13	2.383	$-2.4223110 \times 10^{-3}$	7.0785057×10^{-2}	$-6.4677566 \times 10^{-1}$	7.5971351
14	2.538	$-2.5288548 \times 10^{-3}$	7.3413682×10^{-2}	$-6.6778608 \times 10^{-1}$	8.0313221
15	2.691	$-2.6319780 \times 10^{-3}$	7.5959811×10^{-2}	$-6.8814410 \times 10^{-1}$	8.4757174
16	2.841	$-3.0648121 \times 10^{-3}$	8.6504631×10^{-2}	$-7.7185918 \times 10^{-1}$	1.0538735×10^1
17	2.988	$-3.4839030 \times 10^{-3}$	9.6716406×10^{-2}	$-8.5293179 \times 10^{-1}$	1.3013740×10^1
18	3.132	$-3.8895279 \times 10^{-3}$	1.0660187×10^{-1}	$-9.3141628 \times 10^{-1}$	1.5961770×10^1
19	3.273	$-4.2819173 \times 10^{-3}$	1.1616660×10^{-1}	-1.0073577	1.9448144×10^1
20	3.411	$-4.6612557 \times 10^{-3}$	1.2541506×10^{-1}	-1.0807920	2.3541588×10^1
21	3.546	$-5.1733322 \times 10^{-3}$	1.3767440×10^{-1}	-1.1764885	3.0086266×10^1
22	3.678	$-5.6710521 \times 10^{-3}$	1.4959050×10^{-1}	-1.2694962	3.8183202×10^1
23	3.807	$-6.1541310 \times 10^{-3}$	1.6115663×10^{-1}	-1.3597647	4.8116778×10^1
24	3.932	$-6.6222213 \times 10^{-3}$	1.7236450×10^{-1}	-1.4472310	6.0197090×10^1
25	4.053	$-7.0749031 \times 10^{-3}$	1.8320408×10^{-1}	-1.5318182	7.4752879×10^1
26	4.171	$-7.6231977 \times 10^{-3}$	1.9527363×10^{-1}	-1.6170367	9.0752995×10^1
27	4.284	$-8.1630545 \times 10^{-3}$	2.0718159×10^{-1}	-1.7013496	1.1002371×10^2
28	4.394	$-8.6924335 \times 10^{-3}$	2.1888022×10^{-1}	-1.7843934	1.3308005×10^2
29	4.499	$-9.2090051 \times 10^{-3}$	2.3031537×10^{-1}	-1.8657585	1.6043661×10^2
30	4.599	$-9.7100645 \times 10^{-3}$	2.4142454×10^{-1}	-1.9449751	1.9255701×10^2
31	4.693	$-1.0286822 \times 10^{-2}$	2.5290541×10^{-1}	-2.0154507	2.1943084×10^2
32	4.782	$-1.0857811 \times 10^{-2}$	2.6437935×10^{-1}	-2.0869987	2.5146934×10^2
33	4.865	$-1.0479586 \times 10^{-2}$	2.5238800×10^{-1}	-1.9696590	1.7601956×10^2
34	4.939	$-1.0160843 \times 10^{-2}$	2.4208262×10^{-1}	-1.8676456	1.2879300×10^2
35	5.005	$-9.8993969 \times 10^{-3}$	2.3345767×10^{-1}	-1.7812805	9.8678239×10^1
36	5.060	$-1.0714212 \times 10^{-3}$	2.4212351×10^{-2}	$-1.6419422 \times 10^{-1}$	1.6898127
37	5.099	5.5925329×10^{-3}	$-1.3355121 \times 10^{-1}$	1.0532033	7.9426229×10^{-2}

The above expressions are the Gupta-Yos functional forms proposed by Gupta *et al.* [97] for fitting collision integral data. The fitting is performed by employing the *dgelsy()* linear least-squares routine available in the LAPACK library [101]. Tables I, II, and III provide the values of the coefficients A, B, C, and D corresponding to the $\pi\sigma^2\Omega^{(1,1)*}$ and $\pi\sigma^2\Omega^{(2,2)*}$ collision integrals, and B_{coll}^* for all 38 vibrational levels of O₂, based on the Varga *et al.* [54] set of surfaces. The energy eigenvalue for each vibrational state is also tabulated. A very good coefficient of determination ($R^2 > 0.84$) was obtained for all three collisional quantities, for fits corresponding to each vibrational level, except for vibrational state, $i = 37$ where $R^2 = 0.60$ for the B_{coll}^* fit.

- [1] J. D. Anderson, *Hypersonic and High Temperature Gas Dynamics* (AIAA, Reston, VA, 2000).
- [2] M. J. Wright, D. Bose, G. E. Palmer, and E. Levin, Recommended collision integrals for transport property computations part 1: Air species, *AIAA J.* **43**, 2558 (2005).
- [3] J.-H. Lee, Basic Governing equations for the flight regimes of aeroassisted orbital transfer vehicles, in *Proceedings of 19th AIAA Thermophysics Conference, Snowmass, Colorado* (AIAA, Reston, VA, 1984), p. 1729.
- [4] P. Gnoffo, R. N. Gupta, and J. L. Shinn, Conservation equations and physical models for hypersonic air flows in thermal and chemical nonequilibrium, Tech. Rep. (NASA-TP-2867, 1989), <https://ntrs.nasa.gov/citations/19890006744>.
- [5] C. Park, Assessment of a two-temperature kinetic model for dissociating and weakly ionizing nitrogen, *J. Thermophys. Heat Transfer* **2**, 8 (1988).
- [6] C. Park, Assessment of two-temperature kinetic model for ionizing air, *J. Thermophys. Heat Transfer* **3**, 233 (1989).
- [7] C. Park, On convergence of computation of chemically reacting flows, in *Proceedings of the AIAA 23rd Aerospace Sciences Meeting* (Reno, Nevada, 1985).
- [8] C. Park, Review of chemical-kinetic problems of future NASA missions. I-Earth entries, *J. Thermophys. Heat Transfer* **7**, 385 (1993).
- [9] R. C. Millikan and D. R. White, Systematics of vibrational relaxation, *J. Chem. Phys.* **39**, 3209 (1963).
- [10] J. G. Parker, Rotational and vibrational relaxation in diatomic gases, *Phys. Fluids* (1958–1988) **2**, 449 (1959).
- [11] C. Park, The limits of two-temperature model, in *Proceedings of the 48th AIAA Aerospace Sciences Meeting Including the New Horizons Forum and Aerospace Exposition, Orlando, Florida* (AIAA, Reston, VA, 2010), pp. 1–13.
- [12] M. Panesi, R. L. Jaffe, D. W. Schwenke, and T. E. Magin, Rovibrational internal energy transfer and dissociation of $N_2(^1\Sigma_{g+})-N(^4S_u)$ system in hypersonic flows, *J. Chem. Phys.* **138**, 044312 (2013).
- [13] M. Panesi, A. Munafò, T. E. Magin, and R. L. Jaffe, Nonequilibrium shock-heated nitrogen flows using a rovibrational state-to-state method, *Phys. Rev. E* **90**, 013009 (2014).
- [14] E. Nagnibeda and E. Kustova, *Non-equilibrium Reacting Gas Flows: Kinetic Theory of Transport and Relaxation Processes* (Springer-Verlag, Berlin, 2009).
- [15] E. Kustova and E. Nagnibeda, Transport properties of a reacting gas mixture with strong vibrational and chemical nonequilibrium, *Chem. Phys.* **233**, 57 (1998).
- [16] E. Kustova, E. Nagnibeda, and A. Chauvin, State-to-state nonequilibrium reaction rates, *Chem. Phys.* **248**, 221 (1999).
- [17] I. D. Boyd, G. Chen, and G. V. Candler, Predicting failure of the continuum fluid equations in transitional hypersonic flows, *Phys. Fluids* **7**, 210 (1995).
- [18] T. D. Holman and I. D. Boyd, Effects of continuum breakdown on hypersonic aerothermodynamics for reacting flow, *Phys. Fluids* **23**, 027101 (2011).
- [19] K. Swaminathan-Gopalan, S. Subramaniam, and K. A. Stephani, Generalized Chapman-Enskog continuum breakdown parameters for chemically reacting flows, *Phys. Rev. Fluids* **1**, 083402 (2016).
- [20] S. Subramaniam and K. A. Stephani, Influence of surface chemistry on continuum breakdown in high-speed chemically reacting flows, in *Proceedings of the 47th AIAA Thermophysics Conference, Denver, Colorado* (AIAA, Reston, VA, 2017), p. 4343.
- [21] S. Subramaniam and K. A. Stephani, Assessment of continuum breakdown for chemically reacting wake flows, *Phys. Rev. Fluids* **3**, 123401 (2018).
- [22] G. Bird, *Molecular Gas Dynamics and the Direct Simulation of Gas Flows* (Oxford University Press, Oxford, 1994).
- [23] J. N. Moss and G. A. Bird, Direct simulation of transitional flow for hypersonic reentry conditions, *J. Spacecr. Rockets* **40**, 830 (2003).
- [24] J. G. Kim and I. D. Boyd, Monte Carlo simulation of nitrogen dissociation based on state-resolved cross sections, *Phys. Fluids* (1994–present) **26**, 012006 (2014).

- [25] T. J. Scanlon, C. White, M. K. Borg, R. C. Palharini, E. Farbar, I. D. Boyd, J. M. Reese, and R. E. Brown, Open-source direct simulation Monte Carlo chemistry modeling for hypersonic flows, *AIAA J.* **53**, 1670 (2015).
- [26] S. Gimelshein and I. Wysong, DSMC modeling of flows with recombination reactions, *Phys. Fluids* **29**, 067106 (2017).
- [27] T.-J. Pan, T. J. Wilson, and K. A. Stephani, Vibrational state-specific model for dissociation and recombination of the $O_2(^3\Sigma_g^-) + O(^3P)$ system in DSMC, *J. Chem. Phys.* **150**, 074305 (2019).
- [28] T.-J. Pan, C. Kondur, S. Subramaniam, and K. A. Stephani, A state-resolved recombination model using orbiting cross-sections from the potential energy surface for atomic oxygen in DSMC, in *Proceedings of the AIAA Scitech 2019 Forum, San Diego, California* (AIAA, Reston, VA, 2019), p. 0797.
- [29] T.-J. Pan, S. Subramaniam, C. Kondur, and K. Stephani, A state-resolved DSMC recombination model with orbiting-pair cross-sections, in *31st International Symposium on Rarefied Gas Dynamics: RGD31*, edited by Y. Zhang, D. R. Emerson, D. Lockerby, and L. Wu, AIP Conf. Proc. No. 2132 (AIP Publishing, College Park, MD, 2019), p. 070017.
- [30] T. E. Schwartzentruber and I. D. Boyd, A hybrid particle-continuum method applied to shock waves, *J. Comput. Phys.* **215**, 402 (2006).
- [31] J. M. Burt and I. D. Boyd, A hybrid particle approach for continuum and rarefied flow simulation, *J. Comput. Phys.* **228**, 460 (2009).
- [32] K. A. Stephani, D. B. Goldstein, and P. L. Varghese, A non-equilibrium surface reservoir approach for hybrid DSMC/Navier–Stokes particle generation, *J. Comput. Phys.* **232**, 468 (2013).
- [33] D. Liechty, A. J. Wise, S. Subramaniam, and K. A. Stephani, Comparison of CFD and DSMC using calibrated transport parameters, in *31st International Symposium on Rarefied Gas Dynamics: RGD31*, edited by Y. Zhang, D. R. Emerson, D. Lockerby, and L. Wu, AIP Conf. Proc. No. 2132 (AIP Publishing, College Park, MD, 2019), p. 070016.
- [34] K. Koura, Monte Carlo direct simulation of rotational relaxation of diatomic molecules using classical trajectory calculations: Nitrogen shock wave, *Phys. Fluids* **9**, 3543 (1997).
- [35] T. E. Schwartzentruber, M. S. Grover, and P. Valentini, Direct molecular simulation of nonequilibrium dilute gases, *J. Thermophys. Heat Transfer* **32**, 892 (2018).
- [36] I. Armenise, M. Capitelli, R. Celiberto, G. Colonna, C. Gorse, and A. Laganà, The effect of $N + N_2$ collisions on the non-equilibrium vibrational distributions of nitrogen under reentry conditions, *Chem. Phys. Lett.* **227**, 157 (1994).
- [37] M. Capitelli, I. Armenise, and C. Gorse, State-to-state approach in the kinetics of air components under re-entry conditions, *J. Thermophys. Heat Transfer* **11**, 570 (1997).
- [38] I. Armenise, M. Capitelli, and C. Gorse, Nitrogen nonequilibrium vibrational distributions and non-Arrhenius dissociation constants in hypersonic boundary layers, *J. Thermophys. Heat Transfer* **12**, 45 (1998).
- [39] I. Armenise, M. Capitelli, E. Kustova, and E. Nagnibeda, Influence of nonequilibrium kinetics on heat transfer and diffusion near re-entering body, *J. Thermophys. Heat Transfer* **13**, 210 (1999).
- [40] I. Armenise and E. Kustova, State-to-state models for CO_2 molecules: From the theory to an application to hypersonic boundary layers, *Chem. Phys.* **415**, 269 (2013).
- [41] O. Kunova and E. Nagnibeda, State-to-state description of reacting air flows behind shock waves, *Chem. Phys.* **441**, 66 (2014).
- [42] O. Kunova and E. Nagnibeda, On the influence of state-to-state distributions on exchange reaction rates in shock heated air flows, *Chem. Phys. Lett.* **625**, 121 (2015).
- [43] A. Lagana and E. Garcia, Temperature dependence of nitrogen atom-molecule rate coefficients, *J. Phys. Chem.* **98**, 502 (1994).
- [44] F. Esposito and M. Capitelli, Quasiclassical molecular dynamic calculations of vibrationally and rotationally state selected dissociation cross-sections: $N + N_2(v, j) \rightarrow 3N$, *Chem. Phys. Lett.* **302**, 49 (1999).
- [45] M. Capitelli, F. Esposito, E. Kustova, and E. Nagnibeda, Rate coefficients for the reaction $N_2(i) + N \rightarrow 3N$: A comparison of trajectory calculations and the Treanor-Marrone model, *Chem. Phys. Lett.* **330**, 207 (2000).

- [46] F. Esposito and M. Capitelli, Quasiclassical trajectory calculations of vibrationally specific dissociation cross-sections and rate constants for the reaction $O + O_2(v) \rightarrow 3O$, *Chem. Phys. Lett.* **364**, 180 (2002).
- [47] D. Andrienko and I. D. Boyd, Investigation of oxygen vibrational relaxation by quasiclassical trajectory method, *Chem. Phys.* **459**, 1 (2015).
- [48] D. Andrienko and I. D. Boyd, Rovibrational energy transfer and dissociation in O_2 -O collisions, *J. Chem. Phys.* **144**, 104301 (2016).
- [49] A. J. C. Varandas and A. A. C. C. Pais, A realistic double many-body expansion (DMBE) potential energy surface for ground-state O_3 from a multiproperty fit to *ab initio* calculations, and to experimental spectroscopic, inelastic scattering, and kinetic isotope thermal rate data, *Mol. Phys.* **65**, 843 (1988).
- [50] J. D. Bender, P. Valentini, I. Nompelis, Y. Paukku, Z. Varga, D. G. Truhlar, T. Schwartzentruber, and G. V. Candler, An improved potential energy surface and multi-temperature quasiclassical trajectory calculations of $N_2 + N_2$ dissociation reactions, *J. Chem. Phys.* **143**, 054304 (2015).
- [51] D. W. Schwenke, R. L. Jaffe, and G. M. Chaban, Collisional dissociation of CO: *Ab initio* potential energy surfaces and quasiclassical trajectory rate coefficients, Tech. Rep. (ARC-E-DAA-TN30024, 2016), <https://ntrs.nasa.gov/citations/20160012461>.
- [52] Z. Varga, R. Meana-Pañeda, G. Song, Y. Paukku, and D. G. Truhlar, Potential energy surface of triplet N_2O_2 , *J. Chem. Phys.* **144**, 024310 (2016).
- [53] W. Lin, Z. Varga, G. Song, Y. Paukku, and D. G. Truhlar, Global triplet potential energy surfaces for the $N_2(X^1\Sigma) + O(^3P) \rightarrow NO(X^2\Pi) + N(^4S)$ reaction, *J. Chem. Phys.* **144**, 024309 (2016).
- [54] Z. Varga, Y. Paukku, and D. G. Truhlar, Potential energy surfaces for $O + O_2$ collisions, *J. Chem. Phys.* **147**, 154312 (2017).
- [55] Y. Paukku, K. R. Yang, Z. Varga, G. Song, J. D. Bender, and D. G. Truhlar, Potential energy surfaces of quintet and singlet O_4 , *J. Chem. Phys.* **147**, 034301 (2017).
- [56] T. K. Mankodi, U. V. Bhandarkar, and B. P. Puranik, Dissociation cross sections for $N_2 + N \rightarrow 3N$ and $O_2 + O \rightarrow 3O$ using the QCT method, *J. Chem. Phys.* **146**, 204307 (2017).
- [57] T. E. Magin, M. Panesi, A. Bourdon, R. L. Jaffe, and D. W. Schwenke, Coarse-grain model for internal energy excitation and dissociation of molecular nitrogen, *Chem. Phys.* **398**, 90 (2012).
- [58] A. Munafò, M. Panesi, and T. E. Magin, Boltzmann rovibrational collisional coarse-grained model for internal energy excitation and dissociation in hypersonic flows, *Phys. Rev. E* **89**, 023001 (2014).
- [59] A. Munafò, Y. Liu, and M. Panesi, Modeling of dissociation and energy transfer in shock-heated nitrogen flows, *Phys. Fluids* **27**, 127101 (2015).
- [60] Y. Liu, M. Panesi, A. Sahai, and M. Vinokur, General multi-group macroscopic modeling for thermochemical non-equilibrium gas mixtures, *J. Chem. Phys.* **142**, 134109 (2015).
- [61] A. Sahai, B. Lopez, C. Johnston, and M. Panesi, Adaptive coarse graining method for energy transfer and dissociation kinetics of polyatomic species, *J. Chem. Phys.* **147**, 054107 (2017).
- [62] R. Macdonald, R. Jaffe, D. Schwenke, and M. Panesi, Construction of a coarse-grain quasi-classical trajectory method. I. Theory and application to N_2 - N_2 system, *J. Chem. Phys.* **148**, 054309 (2018).
- [63] E. Kustova, On the simplified state-to-state transport coefficients, *Chem. Phys.* **270**, 177 (2001).
- [64] E. Kustova, E. Nagnibeda, and A. Chikhaoui, On the accuracy of non-equilibrium transport coefficients calculation, *Chem. Phys.* **270**, 459 (2001).
- [65] E. Josyula, E. Kustova, P. Vedula, and J. M. Burt, Influence of state-to-state transport coefficients on surface heat transfer in hypersonic flows, in *Proceedings of the 52nd Aerospace Sciences Meeting, National Harbor, Maryland* (AIAA, Reston, VA, 2014), p. 0864.
- [66] D. Bruno, M. Capitelli, E. Kustova, and E. Nagnibeda, Non-equilibrium vibrational distributions and transport coefficients of $N_2(v)$ -N mixtures, *Chem. Phys. Lett.* **308**, 463 (1999).
- [67] Y. E. Gorbachev, F. J. Gordillo-Vázquez, and J. A. Kunc, Diameters of rotationally and vibrationally excited diatomic molecules, *Physica A* **247**, 108 (1997).
- [68] E. V. Kustova and G. M. Kremer, Effect of molecular diameters on state-to-state transport properties: The shear viscosity coefficient, *Chem. Phys. Lett.* **636**, 84 (2015).

- [69] G. M. Kremer, O. V. Kunova, E. V. Kustova, and G. P. Oblapenko, The influence of vibrational state-resolved transport coefficients on the wave propagation in diatomic gases, *Physica A* **490**, 92 (2018).
- [70] E. Kustova, M. Mekhonoshina, and G. Oblapenko, On the applicability of simplified state-to-state models of transport coefficients, *Chem. Phys. Lett.* **686**, 161 (2017).
- [71] S. H. Kang and J. A. Kunc, Molecular diameters in high-temperature gases, *J. Phys. Chem.* **95**, 6971 (1991).
- [72] H. Luo, S. Macheret, and A. Alexeenko, First-principle calculations of collision integrals for N₂-O system, in *Proceedings of the Joint Thermophysics and Heat Transfer Conference, AIAA AVIATION Forum, Atlanta, Georgia* (AIAA, Reston, VA, 2018).
- [73] F. Esposito and M. Capitelli, The relaxation of vibrationally excited O₂ molecules by atomic oxygen, *Chem. Phys. Lett.* **443**, 222 (2007).
- [74] I. Armenise and F. Esposito, Dissociation–recombination models in hypersonic boundary layer O₂/O flows, *Chem. Phys.* **398**, 104 (2012).
- [75] I. D. Boyd and E. Josyula, Detailed analysis of vibrational nonequilibrium of molecular oxygen in shock-heated flow, *Phys. Rev. Fluids* **2**, 123401 (2017).
- [76] M. S. Grover, T. E. Schwartzentruber, Z. Varga, and D. G. Truhlar, Dynamics of vibrational energy excitation and dissociation in oxygen from direct molecular simulation, in *Proceedings of the 2018 AIAA Aerospace Sciences Meeting, Kissimmee, Florida* (AIAA, Reston, VA, 2018), p. 0238.
- [77] S. Venturi, M. Sharma Priyadarshini, A. Racca, and M. Panesi, Effects of Ab-initio potential energy surfaces on O₂-O non-equilibrium kinetics, in *Proceedings of the AIAA Aviation 2019 Forum, Dallas, Texas* (AIAA, Reston, VA, 2019), p. 3358.
- [78] D. A. Andrienko and I. D. Boyd, High fidelity modeling of thermal relaxation and dissociation of oxygen, *Phys. Fluids* **27**, 116101 (2015).
- [79] M. Kulakhmetov, M. Gallis, and A. Alexeenko, *Ab initio*-informed maximum entropy modeling of rovibrational relaxation and state-specific dissociation with application to the O₂ + O system, *J. Chem. Phys.* **144**, 174302 (2016).
- [80] J. H. Ferziger and H. G. Kaper, *Mathematical Theory of Transport Processes in Gases* (North-Holland, Amsterdam, 1972).
- [81] S. Subramaniam and K. A. Stephani, Computation of state to state transport coefficients using ab initio potential energy surfaces for the O + O₂ system, in *Proceedings of the AIAA Scitech 2019 Forum, San Diego, California* (AIAA, Reston, VA, 2019), p. 1050.
- [82] R. Munn, E. A. Mason, and F. J. Smith, Some aspects of the quantal and semiclassical calculation of phase shifts and cross sections for molecular scattering and transport, *J. Chem. Phys.* **41**, 3978 (1964).
- [83] E. Levin, H. Partridge, and J. R. Stallcop, Collision integrals and high temperature transport properties for N-N, O-O, and N-O, *J. Thermophys. Heat Transfer* **4**, 469 (1990).
- [84] J. R. Stallcop, H. Partridge, and E. Levin, Effective potential energies and transport cross sections for atom-molecule interactions of nitrogen and oxygen, *Phys. Rev. A* **64**, 042722 (2001).
- [85] L. Monchick and E. Mason, Transport properties of polar gases, *J. Chem. Phys.* **35**, 1676 (1961).
- [86] A. Barbe, C. Secroun, and P. Jouve, Infrared spectra of ¹⁶O₃ and ¹⁸O₃: Darling and Dennison resonance and anharmonic potential function of ozone, *J. Mol. Spectrosc.* **49**, 171 (1974).
- [87] S. Shih, R. J. Buenker, and S. D. Peyerimhoff, Theoretical investigation of the cyclic conformer of ozone, *Chem. Phys. Lett.* **28**, 463 (1974).
- [88] G. Colonna and A. Laricchiuta, General numerical algorithm for classical collision integral calculation, *Comput. Phys. Commun.* **178**, 809 (2008).
- [89] S. Subramaniam and K. A. Stephani, Characterization of state-resolved transport for O + O₂ collisions, in *Proceedings of the 2018 AIAA Aerospace Sciences Meeting, Kissimmee, Florida* (AIAA, Reston, VA, 2018), p. 1484.
- [90] See Supplemental Material at <http://link.aps.org/supplemental/10.1103/PhysRevFluids.5.113402> for details on the state-based distance of closest approach, viscosity cross sections, and collision integrals. Tables of vibrationally resolved $\pi\sigma^2\Psi^{(1,1)*}$, $\pi\sigma^2\Psi^{(2,2)*}$ and B_{coll}^* values are also provided.

- [91] M. Capitelli, D. Bruno, and A. Laricchiuta, *Fundamental Aspects of Plasma Chemical Physics: Transport* (Springer, New York, 2013).
- [92] D. L. Bunker, Mechanics of atomic recombination reactions, *J. Chem. Phys.* **32**, 1001 (1960).
- [93] K. Koura, A set of model cross sections for the Monte Carlo simulation of rarefied real gases: Atom-diatom collisions, *Phys. Fluids* **6**, 3473 (1994).
- [94] C. Kondur, S. Subramaniam, T.-J. Pan, and K. A. Stephani, Computation of orbiting cross-sections from ab initio potential energy surfaces for recombination of atomic oxygen, in *Proceedings of the AIAA Scitech 2019 Forum, San Diego, California* (AIAA, Reston, VA, 2019), p. 2282.
- [95] C. Kondur and K. A. Stephani, Molecular recombination pathways of oxygen from quasiclassical trajectory calculations of the O₃ system, in *Proceedings of the AIAA Scitech 2020 Forum, Orlando, Florida* (AIAA, Reston, VA, 2020), p. 1939.
- [96] J. R. Stallcop, H. Partridge, and E. Levin, H-H₂ collision integrals and transport coefficients, *Chem. Phys. Lett.* **254**, 25 (1996).
- [97] R. N. Gupta, J. M. Yos, and R. A. Thompson, A review of reaction rates and thermodynamic and transport properties for the 11-species air model for chemical and thermal nonequilibrium calculations to 30000 K, Technical Memorandum (NASA-TM-101528, 1989), <https://ntrs.nasa.gov/citations/19890011822>.
- [98] S. Subramaniam and K. A. Stephani, State-based transport and scattering properties for the O + O₂ system, in *31st International Symposium on Rarefied Gas Dynamics: RGD31*, edited by Y. Zhang, D. R. Emerson, D. Lockerby, and L. Wu, AIP Conf. Proc. No. 2132 (AIP Publishing, College Park, MD, 2019), p. 150004.
- [99] S. Chapman and T. Cowling, *The Mathematical Theory of Non-Uniform Gases* (Cambridge University Press, Cambridge, 1970).
- [100] J. Bzowski, J. Kestin, E. Mason, and F. Uribe, Equilibrium and transport properties of gas mixtures at low density: Eleven polyatomic gases and five noble gases, *J. Phys. Chem. Ref. Data* **19**, 1179 (1990).
- [101] E. Anderson, Z. Bai, C. Bischof, S. Blackford, J. Demmel, J. Dongarra, J. Du Croz, A. Greenbaum, S. Hammarling, A. McKenney, and D. Sorensen, *LAPACK Users' Guide*, 3rd ed. (Society for Industrial and Applied Mathematics, Philadelphia, 1999).